

UNCLASSIFIED

AD NUMBER

ADB008388

LIMITATION CHANGES

TO:

Approved for public release; distribution is unlimited.

FROM:

Distribution authorized to U.S. Gov't. agencies only; Test and Evaluation; SEP 1975. Other requests shall be referred to Army Ballistic Research Laboratory, Attn: AMXBR-SS, Aberdeen Proving Ground, MD 21005.

AUTHORITY

st-a usaardc ltr, 8 mar 1978

THIS PAGE IS UNCLASSIFIED

THIS REPORT HAS BEEN DELIMITED
AND CLEARED FOR PUBLIC RELEASE
UNDER DOD DIRECTIVE 5200.20 AND
NO RESTRICTIONS ARE IMPOSED UPON
ITS USE AND DISCLOSURE.

DISTRIBUTION STATEMENT A

APPROVED FOR PUBLIC RELEASE;
DISTRIBUTION UNLIMITED.

BRL MIR 2536

B R L

AD

AD B008388

MEMORANDUM REPORT NO. 2536

THE EFFECT OF A SUB-CALIBER CYLINDRICAL
AFTER-BODY ON THE BEHAVIOR OF
SPIN-STABILIZED PROJECTILES

L. C. MacAllister
V. Oskay
B. J. Reiter
R. Klein
W. Gazdayka

DDC
REF ID: A
JAN 9 1976
REF ID: A

September 1975

Distribution limited to US Government agencies only; Test and Evaluation; Ser 75 Other requests for this document must be referred to Director, USA Ballistic Research Laboratories, ATTN: AMXBR-SS, Aberdeen Proving Ground, Maryland 21005.

USA BALLISTIC RESEARCH LABORATORIES
ABERDEEN PROVING GROUND, MARYLAND

Destroy this report when it is no longer needed.
Do not return it to the originator.

Secondary distribution of this report by originating
or sponsoring activity is prohibited.

Additional copies of this report may be obtained
from the Defense Documentation Center, Cameron
Station, Alexandria, Virginia 22314.

The findings in this report are not to be construed as
an official Department of the Army position, unless
so designated by other authorized documents.

*The use of trade names or manufacturers' names in this report
does not constitute indorsement of any commercial product.*

~~UNCLASSIFIED~~

SECURITY CLASSIFICATION OF THIS PAGE (When Data Entered)

TABLE OF CONTENTS

	Page
LIST OF ILLUSTRATIONS	5
I. INTRODUCTION	9
A. Typical Characteristics	9
B. Tests and Evaluation Procedures	11
II. DESCRIPTION OF TEST METHODS	12
III. ANALYSIS OF THE TEST RESULTS	14
IV. AERODYNAMIC BEHAVIOR	16
A. Mach Number Effects at Small Yaw Levels	16
B. Yaw Effects at Small Angles of Attack	17
C. Aerodynamic Behavior at Higher Yaw Levels	19
D. Ballistic Implications of the Test Data	22
V. COMPARISON OF COMPUTER ANALYSES AND YAWSONDE RESULTS	23
VI. SUMMARY	26
ACKNOWLEDGEMENTS	27
REFERENCES	65
LIST OF SYMBOLS	67
DISTRIBUTION LIST	71

LIST OF ILLUSTRATIONS

Figure	Page
1. Schematic of Various Test Models	28
2. Set-up for the High-Yaw Tests	29
3. Shadowgraph of a 107mm Shell at High Yaw	30
4. Schematic of Magnus Test Model	31
5. Reynolds Number vs Mach Number for Wind Tunnel Tests	32
6. A Yawsonde Instrumented 107mm Mortar Shell	33
7. Schematic of the HDL Yawsonde	34
8. Reproduction of a Telemetry Pulse Train	35
9. Drag Coefficient vs Mach Number for a Square-Based Shell with Different Boom Lengths	36
10. Static Moment Slope vs Mach Number for Various Test Models .	37
11. Magnus Moment Slope vs Mach Number for a Square-Based Shell with Different Boom Lengths	38
12. Drag Coefficient vs δ^2 for Various Test Models	39
13. Static Moment Slope vs δ^2 for Various Test Models	40
14. Magnus Moment Slope vs δ^2 for Various Test Models	41
15. Sketch of the Observed Wake for the Square-Based Shell with Long Boom	42
16. Drag Coefficient vs δ for Square-Based Shell	43
17. Drag Coefficient Comparison for Square-Based Shell with Short Boom	44
18. Drag Coefficient Comparison for Square-Based Shell with Long Boom	45
19. Static Moment Coefficient vs δ for Square-Based Shell.	46
20. Static Moment Coefficient Comparison for Square-Based Shell with Short Boom	47

LIST OF ILLUSTRATIONS (continued)

Figure	Page
21. Static Moment Coefficient Comparison for Square-Based Shell with Long Boom	48
22. Static Moment and Normal Force Coefficients vs Yaw for Boattailed Shell	49
23. Static Moment Coefficient Comparison for Boattailed Shell . .	50
24. Lift Coefficient vs Yaw for Various Test Models	51
25. Magnus Moment Coefficient vs Yaw for Boattailed Shell . . .	52
26. Magnus Moment Coefficient Comparison for Boattailed Shell . .	53
27. Magnus Moment Coefficient vs δ for Square-Based Shell . . .	54
28. Magnus Moment Coefficient Comparison for Square-Based Shell with Short Boom	55
29. Magnus Moment Coefficient Comparison for Square-Based Shell with Long Boom	56
30. Damping Factor vs δ^2 for Various Test Models	57
31. Computed Yaw History for the Short-Boomed Square-Based Projectile at Low Elevation and Medium Velocity	58
32. Computed Yaw History for the Long-Boomed Square-Based Projectile at Low Elevation and Medium Velocity	59
33. Computed Yaw History for the Short-Boomed Square-Based Projectile at High Elevation and Low Velocity	60
34. Computed Yaw History for the Long-Boomed Square-Based Projectile at High Elevation and Low Velocity	61
35. Computed Yaw History for the Short-Boomed Square-Based Projectile at High Elevation and Low Velocity with Wind Shear at the Summit	62
36. Comparison of the Computed Solar Aspect Angle History with the Yawsonde Data for the Short-Boomed Square-Based Projectile at High Elevation and Low Velocity	63

LIST OF ILLUSTRATIONS (continued)

Figure	Page
37. Chapman-Kirk Fit to the Angle of Attack Derived from an Instrumented Flight of the Boattailed Projectile	64

I. INTRODUCTION

Occasionally, subcaliber cylindrical extensions (or booms) are attached to the base of a spin-stabilized shell for nonaerodynamic purposes. The 4.2-inch (107mm) mortar shell, in use since 1940, is one of the few field examples. Earlier versions of this shell had an ignition boom 1/3 caliber in diameter and 1.25 calibers long which carried the ignition and propelling charges and provided the necessary chamber volume for this muzzle loading system. Figure 1 shows various projectiles used with this mortar. In the 1950's, changes were made to upgrade the system performance; among these was the addition of an extension to the original boom, bringing the total length to 1.6 calibers. At the design stage, it had been assumed that the boom produces no aerodynamic effects. The ballistic testing of the earlier versions yielded only range and time-of-flight to impact data. Tests comparing the long and short boomed versions of both the older and newer designs suggested that differences in drag and stability did exist for similar projectiles with different boom lengths. In addition, the projectiles with longer booms showed a greater propensity for occasionally erratic flights. These indications of aerodynamic differences, which seemed ascribable to the boom alone, led to more sophisticated tests of the older shell at the Ballistic Research Laboratories. These became interwoven with the testing of newer concepts by Picatinny Arsenal (PA). As various test results began to show that characteristic traits of the longer-boomed shells were only weakly dependent on the basic design, the interests of the research and development agencies became quite mutual. This resulted in an almost equal involvement of PA and BRL in more recent programs. With this combined effort, the scope of testing and evaluation increased; wind tunnel tests, aeroballistic range tests, and free flight testing of shells instrumented with telemetry and yawsondes were carried out in addition to the normal field tests. This comprises rather extensive testing for a subsonic mortar shell.

A. Typical Characteristics

Current spin-stabilized mortar shells are 107mm in caliber. Older shells were typically square-based, about 4.5 calibers long (excluding the boom) and had short ogival heads. Recent designs involve longer ogives and boattails and are quite similar to contemporary artillery shell designs, except for boom.

A spin-stabilized mortar shell is used with a velocity range from 100 to 300 meters/second with elevation angles up to 65°. This variety of launch angle and velocity requirements will cause large variations in the yawing motion (from flights where the yaw could remain near zero to those with summatal yaws exceeding 30°) of the test vehicles discussed below.

When a spin-stabilized projectile goes through the summit, it would fail to trail ideally. The shell will react like a gyroscope in that its axis of symmetry will precess to the right, for the conventional clockwise spin direction, under the influence of the gravitational force. For small yaw conditions and a linear static moment, the complex yaw near the summit is given by^{1,2*}:

$$\text{Yaw of Repose} = -\frac{g d V^{-2} P \cos \theta}{M} \left[1 - i \left(\frac{PT}{M} + \frac{\left(\frac{md^2}{I_y} \right) (C_{Mq})^* - (C_D)^*}{P} \right) \right]$$

where

g is the acceleration due to gravity in ft/sec^2

d is the diameter of the vehicle in feet

V is the vehicle velocity in ft/sec

θ is the trajectory angle with respect to horizontal in degrees

$P = \left(\frac{I_x}{I_y} \right) \left(\frac{pd}{V} \right)$ I_x and I_y are axial and transverse moments of inertia, respectively, in lb-ft^2

p is the projectile spin rate in rad/sec

$M = \left(\frac{md^2}{I_y} \right) (C_{M\alpha})^*$ m is projectile weight in pounds

$(C_{M\alpha})^*$ is the scaled static moment coefficient slope

$i = \sqrt{-1}$

$T = (C_{L\alpha})^* + \left(\frac{md^2}{I_x} \right) (C_{Mp\alpha})^*$ $(C_{L\alpha})^*$ and $(C_{Mp\alpha})^*$ are the scaled lift coefficient and Magnus moment coefficient slopes, respectively

$(C_{Mq})^*$ and $(C_D)^*$ are scaled aerodynamic damping and drag coefficient, respectively

*References are listed on page 65.

The scaled coefficients are defined as $(C_i)^* = \left(\frac{\rho S d}{2m}\right) C_i$

where ρ is the air density in lb/ft^3

$S = \left(\frac{\pi}{4}\right) d^2$ is vehicle reference area in ft^2

In general, the imaginary part of the complex yaw of repose is small in comparison to the real part. Therefore, the major component of the yaw of repose is in the horizontal plane. It is directed to the right of the trajectory and has the magnitude

$$\frac{(gd/V^2) (pd/V)}{(\pi/8) \rho d^5} \left| C_{M_\alpha} \right| I_x \cos \theta$$

From the above relationship, it becomes obvious that the yaw of repose will reach its maximum at or soon after the summit since both the air density and the model velocity are at their minimum while $\cos \theta \approx 1$. For low launch velocities, a tail wind of 20 to 30 knots may augment the already large yaw of repose by ten or more degrees.

At lower launch elevations and higher velocities, one can expect the yaw history to begin with a launch transient containing both yaw frequency modes. Ideally, these damp out to zero until, at the summit, a small right-directed yaw builds up, and then dissolves into a damped transient on the down leg. Such flights can be analyzed on the basis of small-yaw aerodynamics. At higher elevation angles and lower launch velocities, the distance to the summit is short; hence, the launch transient superimposes on the rapidly growing yaw of repose. The summittal yaw will be large; thus, the projectile must recover and damp out the ensuing large transient in order to impact properly. Obviously, large-yaw data are needed for analyses of these cases.

B. Tests and Evaluation Procedures

Types of testing involved have been:

- (1) Tests to obtain time-of-flight and range-to-impact
- (2) Aeroballistic range tests at varying yaw levels up to 40 degrees in the BRL Transonic Range Facility³ with inert shell
- (3) Wind tunnel tests at subsonic and low transonic speeds in the 12-foot Pressure Wind Tunnel of the NASA Ames Research Center⁴ involving several configurations with and without boattails and booms

(4) Free-flight tests of some telemetry-instrumented shells at the Wallops Island facility of NASA⁵, to take advantage of their excellent radar and telemetry receiving equipment.

The boomed, spin-stabilized projectile poses problems for range and wind tunnel testing when Magnus properties at high yaw angles are required. Aeroballistic range tests and the data reduction are convenient only for small yaws, where the linear force/moment system assumptions are realistic. Higher yaw levels can be induced, but the success ratio of the testing decreases while the danger to the installation increases as the required yaw levels go up. The aerodynamic non-linearities associated with the higher yaws can also be handled, but the amount of data needed for good determinations will pyramid rapidly. Wind tunnel Magnus testing of spinning models has been successful in recent years⁶, but very careful test practices and extremely good model and support designs are essential. Subcaliber extensions of the models used in this test program made adequate design and manufacture even more difficult. Since aerodynamic forces on the boom were a relevant part of the force system, the question of isolating the sting-induced effects was critical. The possible problems with the two conventional test modes forced consideration of instrumented flights early in the program, although testing with on-board instrumentation was a relatively new and only a partially tried technique^{7,8,9}.

When the results of the various modes of testing are compared in detail, a great deal more can probably be said about the areas and extent of agreement. However, at the present time, it is quite clear that there is good agreement. It is also strongly indicated that some behavior patterns are attributable primarily to the boom rather than to the basic configuration. This is of more interest than extensive details of an individual design; hence, the report will be directed along these lines.

II. DESCRIPTION OF TEST METHODS

Most of the testing was conventional and only the more exceptional features will be noted for the wind tunnel and the range testing. Instrumented shell testing is less widely known and more details are given.

During the range tests, standard inert shell were fired from a conventional mortar tube adapted to fire horizontally from a light howitzer mount. In the small yaw phases, the random launch yaw levels were accepted. To obtain larger yaw levels, various muzzle attachments usual to the trade were tried. In this case, however, yaw levels above eight degrees were difficult to obtain and more drastic methods were needed. The one which produced high yaws with some degree of reliability and safety consisted of glancing the shell from a 4-

kilogram Lexan cylinder placed about 75 centimeters from the muzzle. The combination of an impulsive torque and the muzzle blast produced yaws over 30° without damage to the projectile. This method was possible because of the rather heavy shell construction and the low velocities. The test set-up and the shadowgraph of a projectile at 37 degrees of yaw are shown in Figures 2 and 3, respectively.

The design features of the wind tunnel model are shown in Figure 4. The test conditions used during the Magnus force and moment tests in the Ames' wind tunnel are indicated on the plot of Reynolds Number versus Mach Number in Figure 5. All aerodynamic coefficients were fitted with fifth order polynomials in the angle of attack.

The test vehicles used for the instrumented flights were also standard inert shell. They differed from those used in the range tests only in that the yawsonde assemblies replaced the fusing whose external configuration they simulated. The yawsondes were developed by the Harry Diamond Laboratories (HDL) for PA from a United Kingdom prototype design⁸. Figure 6 shows one of these instrumented shell.

Figure 7 is a schematic view of the HDL yawsonde, showing its various components. The sensing element is a silicon solar cell mounted parallel to the shell axis. The face of the cell is masked except for two narrow strips which form a "V" with the apex directed toward the nose of the shell. A pinhole on the surface of the assembly forms an aperture. A refractive medium is placed between the pinhole and the solar cell to increase the field of view. The antenna, amplifier, and the RF oscillator are located in the nose of the assembly; the battery pack is to the rear and contains an inertial switch to prevent premature discharging. To operate the switch, both the set-back force and a high spin are required.

During the flight, a small image of the sun (formed by the pinhole) traverses the arms of the "V" once every revolution. The position at which the image crosses depends on the angle between the projectile axis and a line extending to the sun. Thus, the time between successive intercepts of the same arm of the "V", say τ_1 , is a function of the spin rate of the test vehicle; whereas, the time interval between the interception of one arm of the "V" and the interception of the other, τ_2 , is directly related to the solar aspect angle, σ_n . Thus, the ratio $R = \tau_2 / \tau_1$ is a direct measurement of this angle. For the HDL yawsondes, this ratio is limited to a value between 0 and 0.3 by the physical dimensions of the system.

When the sun's image intercepts one of the slits on the surface of the cell, an output voltage results. This voltage is amplified and used for direct frequency modulation of the carrier. The signal is

received by ground antennas and is demodulated prior to recording on the magnetic tape. The recorded pulse train can then be displayed on an oscilloscope film camera for manual measurements or can be fed directly into a computer for automatic reduction. Figure 8 shows a reproduction of such a pulse train obtained from one of the instrumented flights. The top signal is the NASA 36-bit time code while the bottom signal is the pulse train obtained from the silicon solar cell.

During the testing of the instrumented shells, two MPS 19 radars were used to track all rounds. The FPS 16 radar was also available on occasion. Tracking of the high-elevation low-velocity rounds, which barely got out of the ground clutter, was possible only because of the excellence of the Wallops Island radar operators. The existence of the main base telemetry receiving facility also obviated the need for setting up a mobile telemetry system.

III. ANALYSIS OF THE TEST RESULTS

Analysis of the aeroballistic range data utilized conventional techniques which are well documented^{10,11}. Basically, the orientation and position measurements were fitted to closed-form solutions of the linearized equations of motion by differential corrections technique. If the results indicate a linear force/moment system, the process yields the correct stability derivatives directly; if a nonlinear system is indicated, the total results must be reviewed on a quasi-linear basis² to determine the aerodynamic coefficients. Some of the range rounds with higher yaw levels were also simulated with the BRL 6-D program¹² using the final aerodynamic package and the individual initial conditions.

Magnus testing in the wind tunnels has been quite successful in recent years and the analysis of the data for models without afterbodies is straightforward⁶. In this test, however, one of the more important configurational aspects of the model, the boom, was not significantly larger than the model support, see Figure 4. It was believed that the circulatory flow about the rotating boom is a much stronger Magnus force generator than boom-end effects and that the presence of the support would not materially disturb this flow; therefore, meaningful results are possible^{13,14,15}.

Analysis of the data from the instrumented shell flights is new and the techniques are still flexible^{7,9}. The data contained within a pulse train (see Figure 8) must be reduced to a tabulation of solar aspect angle as a function of flight time. This requires the calibration of the pulse ratio R as a function of the solar aspect angle for each yawsonde. For this purpose, the sun is simulated by a beam chopper. The projectile/sonde assembly is mounted in a fixture which permits rotations about the shell axis of symmetry and about an axis perpendicular to it. The axis of symmetry is initially mounted perpen-

dicular to the arc beam, and it is then inclined to simulate the aspect angle. At this inclination, the model is rotated about its axis of symmetry so that the source, imaged through the pinhole, strikes one leg of the "V" on the solar cell and then the other. The inclination of the axis and the roll angle required to intercept both arms of the "V" are recorded, the ratio of this roll angle to 360° is the value of R at that particular aspect angle. Both positive and negative aspect angles are tested to reflect any asymmetries of that particular assembly. For each yawsonde, calibration values of R as a function of the solar angle are fitted by least squares to yield the final calibration curve. This is used to compute the solar aspect angles as a function of flight time from the corresponding values of R measured from the data of an actual test flight⁹.

For tests with low spin rates, short flight times, or noisy data, the yawsonde signals must be measured manually. The pulse train for such flights is reproduced on a 35-mm film and measured using a tele-reader. The solar aspect angles are then calculated by a digital computer. This procedure is very tedious for long flight times. Therefore, the data from such flights are directly reduced using the BRL hybrid computer (EAI 690). The original magnetic tape is played back through a discriminator into the analog section of the computer. The pulse train is used to initiate integrator voltages at the arrival of the two successive pulses, the value of the ratio R is determined. At present, the hybrid computer cannot decode the NASA time coding, and it is necessary to superimpose readings from the computer's internal clock on the data output tape to provide a time base. The time measurements of the internal clock start from the initiation of the computer and must be referenced to the actual flight time. To do this, a portion of the telemetry data is reproduced on film and the start of the measurable data is determined. The zero of the superimposed computer time is expected to be within 0.2 second of the start of the measurable data.

Given the solar aspect angle, ideally it should be possible to subtract the trajectory angles, the solar position and the wind angles, and, hence, to obtain the actual yaw history. In reality, the solar aspect angle data are only one-dimensional; that is, only the semi-apex angle of a conical surface on which the axis of the shell must lie is given. From such data, the trajectory angle (obtained from radar), the moving sun position, and the wind effects can be subtracted only with some ambiguity. Several groups working with such data at the moment are attempting to obtain a unique computer solution. Various techniques employed start with some assumed value of the aerodynamic coefficients and their dependence on yaw and Mach number and the initial conditions of the flight. Through comparisons of the computed solar aspect angles and the actually obtained values, the assumed quantities are varied until a satisfactory convergence of the computation and the measurements are reached. In this paper, the results from both a 6-D simulation operating under manual control and a differential equation fit under computer control¹⁶ are discussed.

The BRL 6-D simulation program¹² uses coordinate axes which are equivalent to a body-fixed non-rolling system. The static aerodynamic forces are represented as drag along the velocity vector and lift normal to it. In this coding, the force and moment systems are represented through appropriate vectorial relationships. The aerodynamic coefficients are expressed as functions of Mach number and the square of the yaw. To obtain the required values of the aerodynamic forces and moments, a two-way linear interpolation technique is used.

On the other hand, the method of Chapman and Kirk¹⁶ fits the differential equations to the observed angular motion by adjusting the aerodynamic coefficients. This procedure has been modified to analyze both the spark range test data and the yawsonde results. Samples of both types of analyses will be discussed in the following section as applicable.

IV. AERODYNAMIC BEHAVIOR

The effects of Mach number and yaw level on the aerodynamics, as determined from both the aeroballistic range and the wind tunnel, and their ballistic implications are discussed in this section. These results are then utilized in the next section to calculate the shell performance, which is then compared with the data obtained from the instrumented flights.

A. Mach Number Effects at Small Yaw Levels

The zero-yaw drag coefficient, C_{D_0} , of the square-based projectile, as obtained from the range tests, is shown in Figure 9. The average yaw level is three degrees, and only the bands encasing the data are shown. The highest band is based on the few no-boom models with the band width indicating the possible scatter based on previous test experience. The test data for short-boom projectiles lie between the no-boom data and a value about 6% lower in the low velocity regions. The data for the long-boom version are found within a band 5% to 15% below the no-boom data in the same velocity region. Above Mach number 0.6, the test data for the two projectiles with booms depart further from the no-boom values and have an increased region of overlap. This trend reverses at about Mach 0.75; the data for both boomed versions approach the no-boom values and both the scatter band and the difference between the two boomed types decrease.

The static moment slope is shown in Figure 10. A typical scatter band for the no-boom results and the actual bands for the others are shown. The no-boom data indicate the smallest value of the overturning moment. The data for the short-boom rounds are slightly higher and show a different trend above Mach 0.6. The differences between the no-

boom and the short-boom case at low Mach numbers and at Mach 0.8 could be accounted for by the center of mass difference. That is to say, at the same center of mass location, these shells would have the same C_{M_α} value

except in the region $M = 0.55$ to 0.75 . The data for the shell with extension lie well above the short-boom results and the correction for the center of mass difference is negligible. Its data scatter is several times larger and the Mach number trend of the results is different. The value of C_{M_α} decreases with increasing Mach number; thus, the differences

between the shell with extension and the other two types decrease at low transonic speeds, analogous to the behavior of the drag coefficient.

The Magnus moment slope, C_{M_p} , is presented in Figure 11 for small yaw values.

Part of the apparent scatter in the long-boom results is due to a high yaw sensitivity discussed later. The few no-boom data show a small negative value and the data for the short-boomed version have a nearly zero value, but sizable positive values are obtained for the long-boomed projectile. Above Mach 0.7, the results for all types tend to converge.

The remaining properties show similar behavior as functions of Mach number; the largest differences are at Mach 0.6 and below, and the differences between various types decrease above Mach 0.7.

B. Yaw Effects at Small Angles of Attack

Three of the aerodynamic properties, C_D , C_{M_α} , and C_{M_p} , which showed distinctive variations with increasing angle of attack in the small yaw region, are illustrated in Figures 12, 13, and 14.

Figure 12 shows the variations of the drag coefficient for a blunt square-based projectile, a long-ogive square-based shell, and a boat-tailed version of the latter. In all cases, the longer boom yields a lower drag level at zero yaw and the increments for various types are similar. In those cases where results for the boomless shell were available, there is only a small difference between them and the results for the short-boomed models.

The static moment coefficient slope, C_{M_α} , corrected for small center of mass differences, is shown in Figure 13. A trend similar to that of the drag coefficient exists. However, in this case, the overturning moment is considerably larger for the long-boom projectile than for the boomless shell, but again the incremental differences for the various basic types are similar. The differences for various

boomed configurations decrease markedly with the increasing yaw level. The small-yaw C_{M_α} of the boattailed projectile agree well with the

slope measured in the aeroballistic range at the same test Mach number as used for the wind tunnel tests. The previously noted boom effect is also obvious for this type projectile.

One of the most interesting variations, the Magnus moment slope, is shown in Figure 14. Values for both the boomless and the short-boomed versions are small for all yaw levels. There is a large positive increment in the value of C_{M_α} for all the long-boomed models. The

value of the effective slope is decreasing rapidly with the increasing yaw and it approaches that of the shorter-boomed models for yaw levels above about five degrees. The indicated variation for Magnus moment must include at least an α^5 term to represent this behavior, even over this small yaw range.

The behavior of other properties are summarized below:

- (1) The lift curve slope, $C_{L_{\alpha_0}}$, of the longer-boomed projectiles is about 20% lower than that of the shorter-boomed types. The differences decrease with the increasing yaw level.
- (2) The damping moment slope sum, $C_{M_q} + C_{M_\alpha}$, was distinctly higher for the long-boomed models, on the order of 30-50%.

There are four main features of the small yaw results: first, the addition of a short boom produces little change in the aerodynamics while the longer boom produces very definite changes even at the smallest yaws; second, the aerodynamic properties of the no-boom and the short-boom types are linear up to eight degrees of yaw, but the longer boom produces highly nonlinear variations; third, the differences caused by the long boom decrease with increasing yaw levels; and fourth, the individual round-to-round variations of the data are noticeably greater for the longer-boomed shell.

In view of the distinctive differences in aerodynamics, one would expect a visible flow difference in the after-body region. The usual shadowgraphic records from the Transonic Range stations are about 35:1 photographic reductions of the 3.5 x 3.5-meter screens. Therefore, details of the subsonic wake could not be recorded clearly. Examination of a large number of plates for the short-boomed projectile never suggested that the near wake was other than a dead-water region. In a very few cases, there was direct evidence that a rearward flow existed along the extension, together with a counter-current nearer to the base,

for the long-boomed shell. It could not be determined whether this was peculiar to these few rounds or if it is true more generally, but could only be detected under the most favorable conditions. It is tempting to assume that it is more general, since this will furnish a mechanism for both the direct effects and the greater variability which were observed for the shells with an extension. A sketch of the wake region as suggested above is shown in Figure 15.

C. Aerodynamic Behavior at Higher Yaw Levels

Most of the high yaw testing of the blunter square-based projectiles were performed in an aeroballistic range, with some confirmation from the yawsonde results. On the other hand, for the boattailed model with longer ogive, there have been extensive wind tunnel tests, some range tests, and again some sonde data. The only flight region where these projectiles can develop high yaws, due to trajectory or high wind conditions, is below Mach 0.5. Therefore, only this lower speed regime is considered in the discussion.

Figure 16 shows the variation of the drag coefficient obtained during the range tests of the square-based shell. The determination of the data is good to about 25° , $\delta = 0.4$; the sparse and more poorly determined data above this region make that portion of the curve more speculative. The drag coefficients of the two boomed versions are different up to $\delta = 0.07$, about 4° , while the no-boom data remain distinct up to 18° , $\delta = 0.30$, the highest test point for this configuration. Several of the high-yaw rounds from the spark range tests of the square-based projectile have been reduced by the method of Chapman and Kirk by Whyte and Jeung of General Electric¹⁷. Figures 17 and 18 show comparisons of Chapman-Kirk analyses with spark range data for the short-boom and long-boom projectiles, respectively. The solid curves are the repeat of the range results from Figure 16 whereas the points were computed from the quadratic drag determination of Whyte for each individual round. In both cases, the quadratic representation of drag gives a good approximation, especially for the short-boomed projectile, to the more complicated drag variations. But beyond a yaw level of about 25° , $\delta^2 = 0.18$, the quadratic drag determination overestimates the value of the coefficient.

The variations of the static moment coefficient, C_M , of the square-based shell are shown in Figure 19. The most distinctive feature of the figure is the strongly nonlinear behavior of the static moment coefficient for the long-boomed projectile. These nonlinearities are so strong that, although the long-boomed shell has the highest static moment at lower angles of attack, its static moment is lower than that of shorter boomed version at yaw levels above 25° ($\delta = 0.40$). The range data indicate a decrease of 25% in the static moment coefficient slope, $C_M \equiv C_M / \sin \alpha$, by 45° yaw and suggest possible static stability by 70° . As a result,

the long-boomed projectile will have extremely high gyroscopic stability at large summits yaw conditions. On the other hand, both the short-boomed and the no-boomed shells appear to have linear static moment coefficients although at the maximum test yaw levels, the static moment coefficient of the short-boomed projectile is beginning to become nonlinear. The nonlinearities of this coefficient and the yaw levels where the coefficient becomes nonlinear are, presumably, associated with the direct influence of the cross flow on the boom.

In Figure 20 we compare the composite range results of static moment coefficient for the short-boomed projectile with the points computed from Chapman-Kirk analysis. Whyte has attempted to represent the static moment as a pentic in δ . His results compare favorably with the range data up to 14° . At yaw levels above 14° , where range data show a tendency to flatten, his values continue to increase. A similar effort for the long-boomed shell is shown in Figure 21. For this shell, whose static moment coefficient is even more nonlinear than the short-boomed version, the best a pentic representation can do is to give the average trend of the range data.

The strong nonlinearities in the aerodynamic system of the boattailed projectile are quite evident in the results of the differential equation fits to the angular motion recorded by the yawsonde and range tests as well as the wind tunnel data. The aerodynamic coefficients obtained from all sources correlate reasonably well. Figure 22 shows the wind tunnel and the range results for the static moment and the normal force coefficients for the boattailed shell. The wind tunnel and the aeroballistic range data at similar Reynolds number compare quite favorably, but the wind tunnel tests have also indicated a Reynolds number effect which as yet cannot be explained.

In Figure 23, static moment results of the Chapman-Kirk analysis of one of the range test firings are compared with the composite range results previously given in Figure 22. The cubic representation of the static moment coefficient used in the Chapman-Kirk analysis agrees well with the range data.

The lift coefficients, as determined from various sources, for both the boattailed and the square-based projectiles are shown in Figure 24. With the exception of the small yaw behavior of the long-boomed model, the lift curves are increasing cubically to about 25° yaw. A small quintic counter-acting variation in the lift coefficient is suggested by the data points at highest yaw levels. Although the wind tunnel and the range results are well determined, the instrumented flights could not furnish a confirmation of any of the details of these results since the lift coefficient influences only the average trajectory.

Both the aeroballistic range and the wind tunnel tests indicated that the Magnus moment of the boattailed design is negative between 7° and 15° angle of attack at a Mach number of 0.55 (see Figure 25). The

negative Magnus moment operating on the projectile will result in a limit cycle in the precessional mode and thus a shorter range. This limit cycle can be predicted by the method of Reference 2. Therefore, tests at $M = 0.55$ were scheduled. As shown in Figure 25, C_{M_p} is below

0.05 up to 16° where a rapid increase is observed. On the other hand, the wind tunnel tests of the boomless boattailed design at $M = 0.55$ give negative Magnus moment coefficient. It is apparent that, at yaw levels above 16° , a circulatory flow is established about the boom.

The wind tunnel tests of the boomed boattailed model at $M = 0.3$ give a low but positive value for the Magnus moment, whereas the boomless version has a nearly linear Magnus moment as a function of angle of attack ($C_{M_p} = 0.5/\text{rad}$) up to 22° at the same Mach number. There-

fore, without a boom, this projectile would be dynamically unstable throughout the angle of attack range since the center of pressure of the sufficiently large Magnus force is forward of the shell's center of gravity.

Figure 26 shows the comparison between the range results, the solid line, and the Chapman-Kirk analyses of two range tests, the diamonds and the circles. Both Chapman-Kirk analyses predict the sign change in the Magnus moment at about 7° yaw level, but the limited yaw base of the smaller-yaw round, the diamonds, permitted only a cubic representation during the Chapman-Kirk analysis and as such the validity of the results beyond 8° yaw level is questionable. On the other hand, the second round had sufficiently large yawing motion to permit the use of a pentic representation of the Magnus moment. As a result, it predicts a second sign change in the Magnus moment at $14^\circ - 15^\circ$ yaw level. The yaw trend of the Magnus moment for the boattailed projectile is well defined by the Chapman-Kirk analyses but the absolute values obtained through this procedure are different from the range results.

Aeroballistic range tests of the square-based projectile gave Magnus data similar to those of the boattailed shell, see Figure 27. Once more, the high yaw behavior of the shell seems to be dominated by the cross-flow acting on the boom to develop a strong Magnus force. Naturally, this occurs for the longer-boomed shell at smaller yaw levels, but the shorter boomed version has similar behavior. The long-boomed shell reaches large positive values of Magnus moment above 18° ($\delta = 0.3$) while the shorter-boomed projectile has an equivalent value of Magnus moment only above 25° ($\delta = 0.42$).

Figures 28 and 29 show comparisons of Magnus moment results for the square-based projectile as obtained from range tests and Chapman-Kirk analyses. Figure 28 shows the comparison for the short-boomed shell. Although the pentic (α^5) approximation to the Magnus moment has generally the same trends as the range results, at small yaw levels, say

below 15°, it is at best an average of the actual range results. On the other hand, the large yaw behavior predicted by Chapman-Kirk analyses deviates strongly from the range results in that the steep rise of the Magnus moment starts about 4° prior to the range indications and increases more rapidly than the test results. Figure 29 is a similar comparison for the long-boomed shell where three test firings have been analyzed by Chapman-Kirk method for comparison due to yaw limitations of each individual round. In its basic features this figure is quite similar to Figure 26 for the boattail projectile in that: (a) low-yaw rounds, the circles and the triangles, are able to predict only the first sign change of the Magnus moment, (b) the high yaw round could predict the second sign change but it is not correct at lower yaws, (c) the trend of the Magnus moment coefficient predicted by the combined results of the Chapman-Kirk analyses is in agreement with the range test data, and (d) the absolute values of the Magnus moment computed from Chapman-Kirk analyses differ drastically from the composite range results.

The few high yaw test indicated that in this region the damping moment coefficient sum $(C_{M_q} + C_{M_\alpha})$ remains relatively constant, lying between -3 and -5; hence, during the simulation analyses, the value of this coefficient at the high end of the small yaw data was used. No discrepancies were observed.

D. Ballistic Implications of the Test Data

The implications of the high yaw data on ballistics are more properly discussed in conjunction with the 6-D analyses of the next section. The effects of smaller yaw levels are submerged in the large yaw behavior, however; therefore, the implications of the small yaw behavior will be mentioned separately.

The aerodynamic forces and moments about the center of mass of the projectile interact with the inertial properties of the vehicle to produce its dynamic behavior characteristics. In principle, the inertial properties are at the disposal of the designer and the result can be tailored to fit the needs in spite of the aerodynamic characteristics. In practice, this latitude is limited for the usual ordnance projectiles since effectiveness or cost penalties generally interfere. Various shell modifications mentioned so far represent a sizable part of the readily available options, resulting in generally similar inertial properties. Therefore, the changes in the boom length will produce equivalent alterations in the behavior of various shell designs.

The lower drag of the longer-boomed projectile would appear to be an advantage since it could translate into longer ranges, but this is not quite the case. Comparison of the ranges calculated from the firing tables for the two configurations of the square-based shell at

the same velocity and weight indicated that: (a) the maximum gain in impact range is equivalent to a reduction of 6% in C_D rather than the maximum possible value of 12% predicted by the aerodynamic testing, (b) at medium angles of elevation, the gain in range corresponds to an effective drag reduction of only 1 to 2%, and (c) at high elevations the trend actually reverses and the longer-boomed shell acts as if it has a drag level 4% higher than that of the short-boomed version.

The reason for this behavior is as follows. The gyroscopic stability of a shell and the magnitude of its yaw of repose, as we have seen in Section I-A, are governed by the projectile's static moment coefficient. For the same center of mass position, the shell with the longer boom has a higher C_{M_α} , therefore, it will have a lower gyroscopic stability. On the other hand, the dynamic behavior of a shell is strongly influenced by its Magnus moment coefficient. Although other aerodynamic properties of the projectile also affect the level of the exponential damping factors, λ_i , the Magnus moment dominates the high frequency mode of these projectiles. The damping factors measured from the range tests are shown in Figure 30. For all the long-boomed versions, the indicated value at zero yaw level represents a divergence of the yaw. The values change as the yaw level increases and the Magnus moment decreases, until at yaw levels of 3° to 6° , depending on the particular design, the indicated value becomes stabilizing. Thus the long-boomed projectiles, at least under these conditions, will not fly at zero yaw. This tendency to fly at a small non-zero yaw coupled with the yaw sensitivity of the aerodynamic properties of the long-boomed shell reduces the behavioral differences between the two types in actual use; in particular, the apparently quite favorable drag difference.

V. COMPARISON OF COMPUTER ANALYSES AND YAWSONDE RESULTS

Figures 31 to 37 show computed behavior of various shell types along sample trajectories. Most of the figures give the magnitude of total yaw as a function of time, which may be readily converted to any desired trajectory parameter. Whenever yawsonde results were available for conditions similar to those used in the computations, then the solar aspect angle is used for comparison of the test results with the computed values, again using the time along the trajectory as independent variable.

Figures 31 and 32 show the computed yaw histories of the short- and long-boomed square-based projectiles, respectively, along a trajectory of low elevation angle and medium velocity. The performance of the no-boom configuration along the same trajectory was also computed, but its behavior showed basically the same trend as the short-boomed shell. Therefore, the results for the no-boom version are not given as a separate figure. The characteristic behavioral differences

at small yaw for the two configurations are quite discernable in the figures. The short-boomed model damps out both the launch transient and the summatal perturbation to essentially zero level by the time of impact, but the long-boomed vehicle is maintaining a high frequency mode throughout its flight. For this long-boom case, the amplitude of the total yaw is increasing up to the summit under the influence of the yaw of repose, but on the down-leg of the trajectory a nearly constant value of total yaw level is maintained although the amplitude of the high frequency mode is decreasing.

Figures 33 and 34 show the computed yaw behavior of the square-based projectile along a trajectory with high gun elevation and low velocity for two boom lengths. Once more, the no-boom results are not shown since they are very similar to those of the short-boom shell. The higher gun elevations at lower speeds create flight conditions which truly differentiate the performances of various configurations. Along these trajectories, the summit is reached sooner, and part of the launch transient is carried into the summit region.

For the short-boomed projectile, Figure 33, the launch transient has already been damped out to a large extent before the top; thus, through the summit the resultant aerodynamic yaw is almost a pure response to the turning of the trajectory induced by the gravity vector and the inertial lag of the shell. A post-summatal fast mode appears and grows briefly as the projectile senses yaw levels over 12° in coming out of the summatal area with a large slow mode. Now it is a race between the small amplitude fast mode which is diverging at these yaw levels and the large slow mode which is damping, but it is clear that the down-leg is dominated by the damping of the low frequency mode. This flight is well behaved near the terminus, both yaw modes damping, from the exterior ballistician's point of view. However, the yaw levels could be large enough to disturb other facets of performance.

Figure 34 shows the yawing history of the long-boomed model under flight conditions similar to that of Figure 33. Here, the high frequency mode resulting from the launch transient is borne into the summit region. Although this mode is damping out, it still has enough amplitude at the summit to provide sufficient excitation for the divergent mode just after the summatal maneuver. The amplitude of this divergent mode is comparable to that of the damped low frequency mode, and near the impact the undamped high frequency mode becomes the controlling factor, as shown in the figure. Therefore, the yaw level remains relatively high until the flight is terminated by impact since the shell cannot recover by itself.

Figure 35 gives an indication of what could happen if a large disturbance is introduced near the summit of the trajectory of the short-boomed projectile. This figure was obtained by combining a high wind condition with maximum tip-off condition (observed during the instrumented flights and range tests, respectively) in an unfavorable manner. Otherwise, this computation is for the same trajectory conditions as

those of Figure 33 with which it may be compared. Now the wind shear has amplified both of the frequency modes before reaching the summit. The down-leg of the motion is quite similar to that of the longer-boomed shell with less disturbance in that near the impact the undamped fast mode is governing the amplitude of the total yaw level of the motion and the shell is nearly destabilized.

During the testing of the instrumented shells, one set of yawsonde data was obtained for the short-boomed version of the square-based shell at a high elevation angle and a low velocity. A comparison of the solar aspect angles obtained during this flight (shown as dashed lines) and the curve calculated by the 6-D simulation of this test is shown in Figure 36. This test firing had taken place soon after the passage of a cold front, hence, under fairly severe wind conditions. Inclusion of this wind profile in the 6-D simulation showed that the large amplitude precessional motion at the beginning of the flight is caused mainly by the wind and its changing profile. The trend of the data obtained by the yawsonde is very closely simulated by the computed curve. It is believed that the exact period of precession and the growth of the nutational motion of the shell could be matched without resorting to major changes in the aerodynamic properties discussed above, by choosing proper initial conditions and a closer approximation to the gusty wind profile near the summit (between 8 and 12 seconds of flight time).

Aerodynamic data discussed in the previous section indicated that the boattailed model is less prone to disturbances by the Magnus effects at higher yaw levels as the result of a deliberate effort to counterbalance these effects by the maximum shift in the inertial and aerodynamic factors. This effort was successful in postponing the onset of the high-yaw instability; however, it has introduced a more complicated small-yaw interaction. The Magnus moment affects the two frequency modes differently. An effort to reduce the effect of this moment on one mode often increases its effect on the other. Both the range and the wind tunnel results indicated that the boattailed model can be precessional unstable in the 6-10° yaw range for some Mach numbers. The raw data obtained from the instrumented flights of the boattailed model suggest the presence of a small amplitude slow mode. Figure 37 shows a fit to a portion of the data obtained from one of these flights. This fit was obtained through the method of Chapman and Kirk. To date, this method has been successfully applied to flights along trajectories where the effects of the yaw of repose and the trajectory curvature are minimal. Thus the data shown in Figure 37 is from a portion of the trajectory prior to the summit. The first step in the Chapman-Kirk method is to remove the trajectory effects from the solar aspect angle data through a 6-D computation. This reduces the test data to an angle of attack history which is then fitted by the Chapman-Kirk method to obtain improvements to the values of the aerodynamic coefficients. The comparison of the coefficients obtained

via Chapman-Kirk fit of this flight and the values obtained through other test methods is given in the following table.

Table I. Comparison of Aerodynamic Coefficients
(Mach Number = 0.85)

Coefficient	Wind Tunnel (Ref: 18)	Spinner Range	Ballistic Linear Term	Cubic Term	Chapman - Kirk Analysis		Value at Probable Avg. Yaw Error (rad)
					Probable Avg. Yaw Error (rad)		
$C_{M\alpha}$	3.0	3.2	3.2	1.80	1397	3.1	.00058
C_{Mq}	---	- 10.0	- 6.0	- 9.7	---	---	.00058
$C_{Mp\alpha}$	- .2	- .2	.2	.5	---	---	.00058

VI. SUMMARY

The addition of a subcaliber after-body to the base of a spin-stabilized projectile produces definite aerodynamic effects, particularly if the boom length exceeds about one caliber for a 1/3 caliber diameter boom. Comparative testing of several types of projectiles, both square-based and boattailed, showed the following effects at small yaw levels as a function of boom length.

- (1) $C_{D\alpha}$ decreases up to 12% for the short boom lengths and up to 28% for the longer boom lengths.
- (2) $C_{M\alpha}$ increases a small amount with the addition of the shorter boom, but up to nearly 50% with the addition of the longer version.
- (3) $C_{L\alpha}$ decreases about 20% for the longer-boomed shell.
- (4) $C_{Mp\alpha}$ for the longer-boomed projectiles is larger than the values for the shorter-boomed versions.

In all cases, longer-boomed shell showed nonlinear aerodynamic behavior, as opposed to the nearly linear aerodynamic behavior of the shorter-boomed types. In general, these nonlinearities acted to decrease the differences between the long- and the short-boomed shell as the yaw level increased, up to yaw levels of about 8°.

At the higher yaw levels, the booms act to decrease the static moment of the basic projectile and also to produce a large positive Magnus moment contribution. Both of these effects appeared to occur once the yaw level reached a point where the boom is in a definite cross-flow. The existence of a large Magnus moment places a limit on the maximum yaw level that either boomed projectile can reach without becoming dynamically unstable.

ACKNOWLEDGEMENTS

The authors would like to express their appreciation to the operations personnel of both NASA Ames Research Center and NASA Wallops Island Test Facility for their able assistance during various stages of testing.

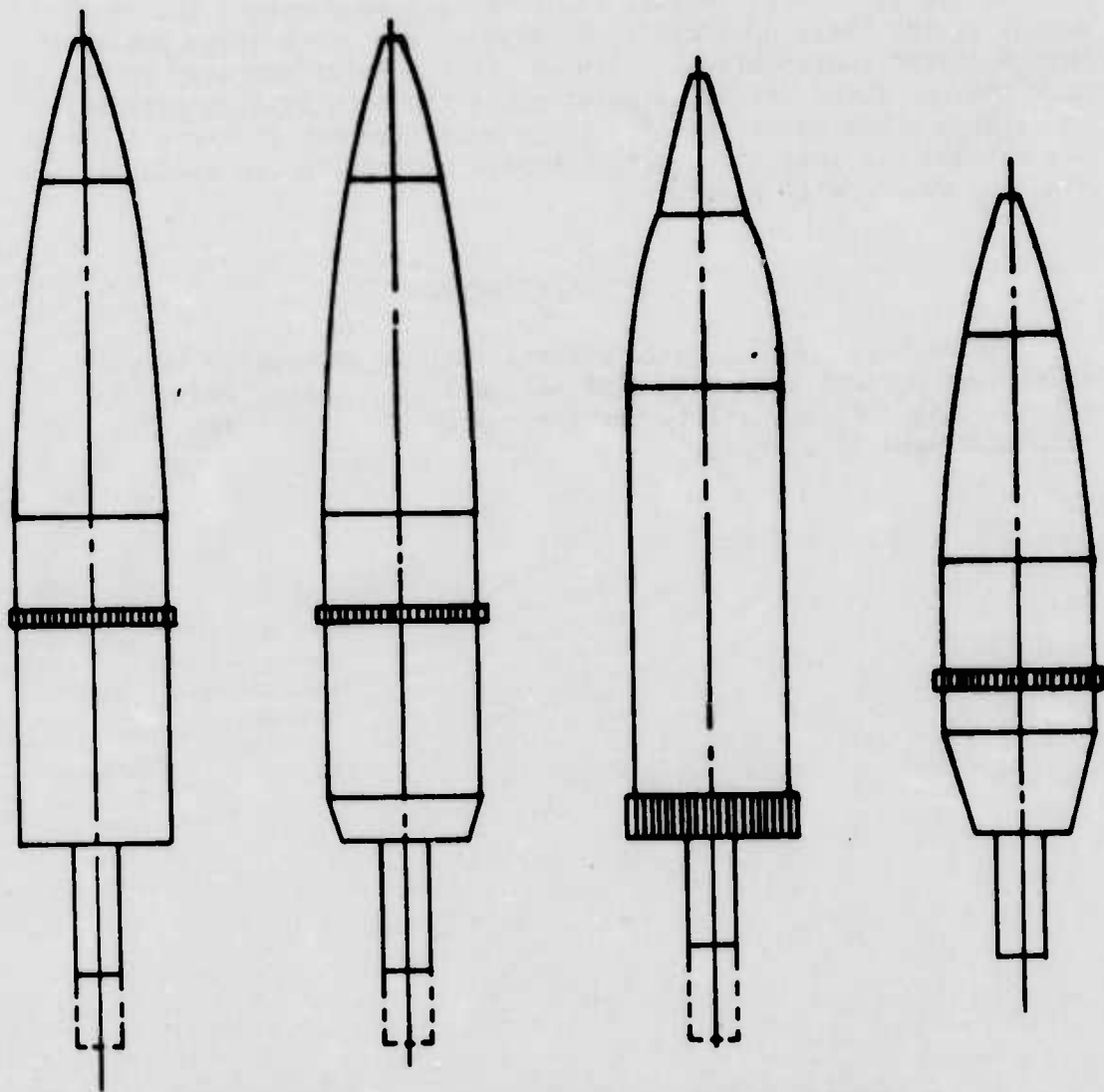


FIGURE 1 SCHEMATIC OF VARIOUS TEST MODELS



Figure 2. Set-up for the High-Yaw Tests



Figure 3. Shadowgraph of a 107mm Shell at High Yaw

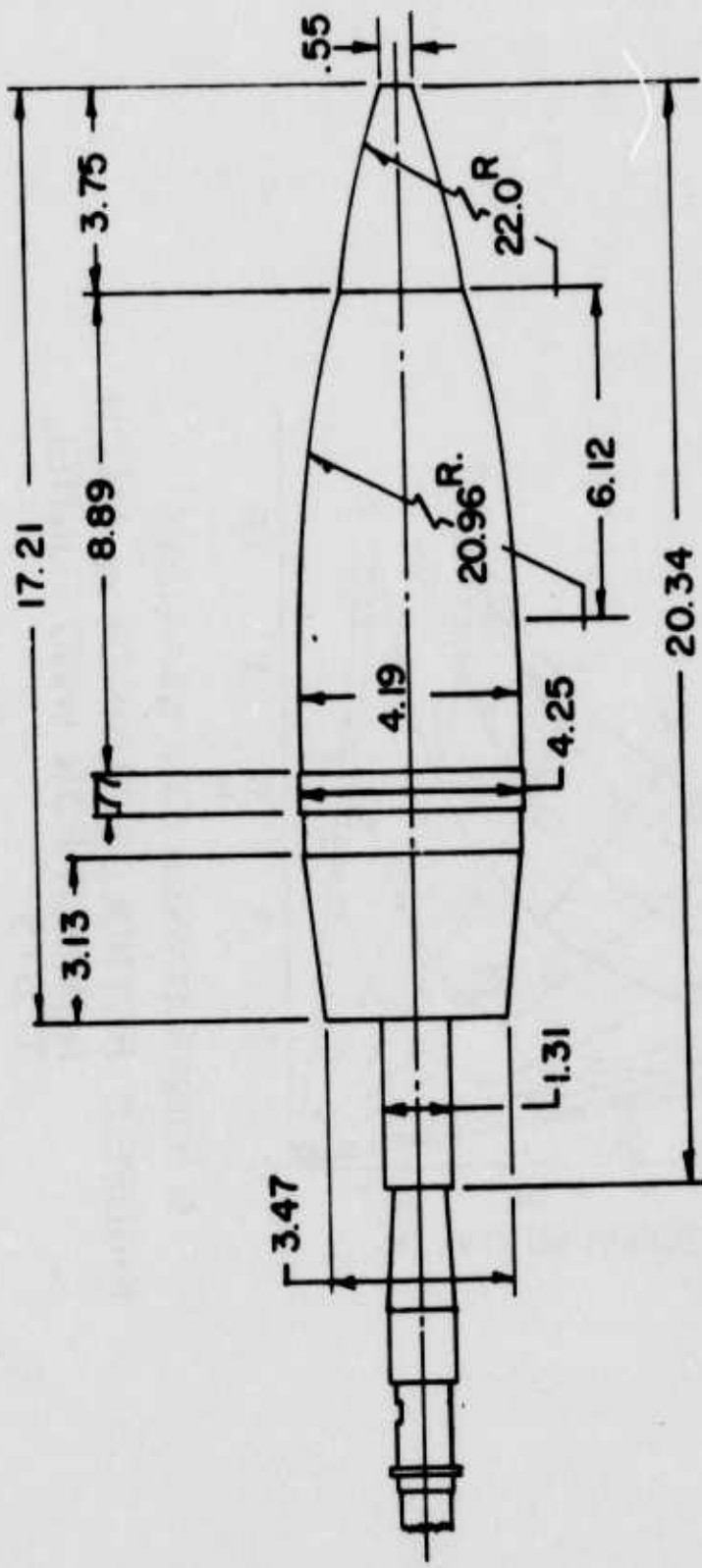
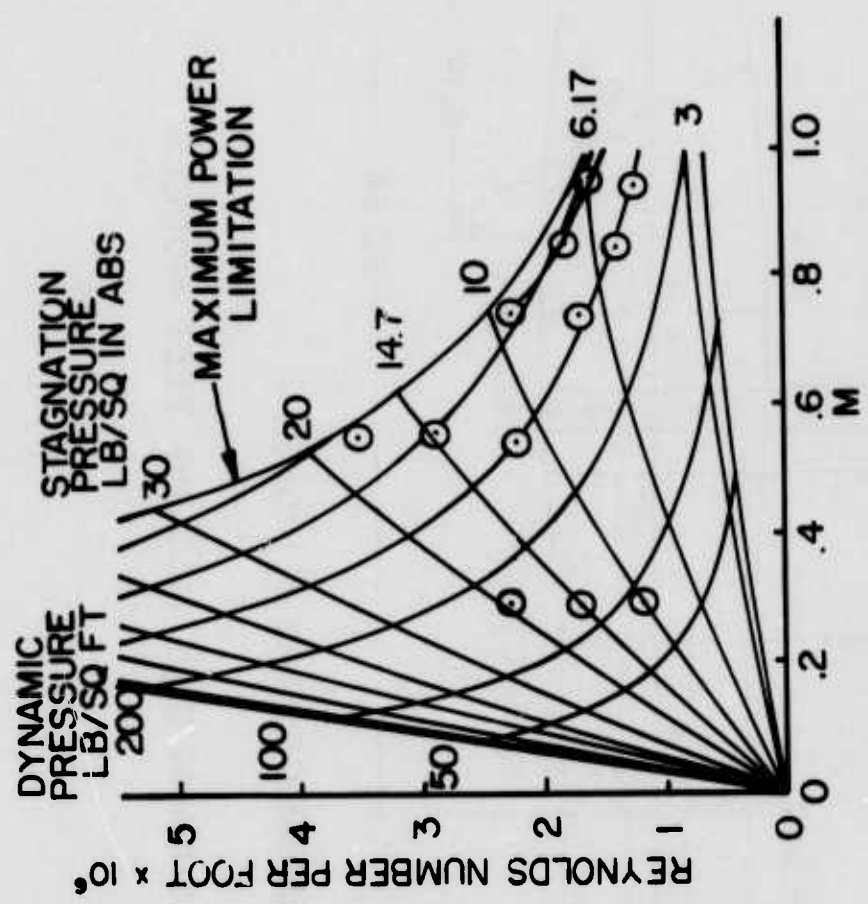


FIGURE 4 SCHEMATIC OF MAGNUS TEST MODELS



○ POINTS AT WHICH DATA WAS TAKEN

FIGURE 5 REYNOLDS NUMBER vs MACH NUMBER FOR WIND TUNNEL TESTS

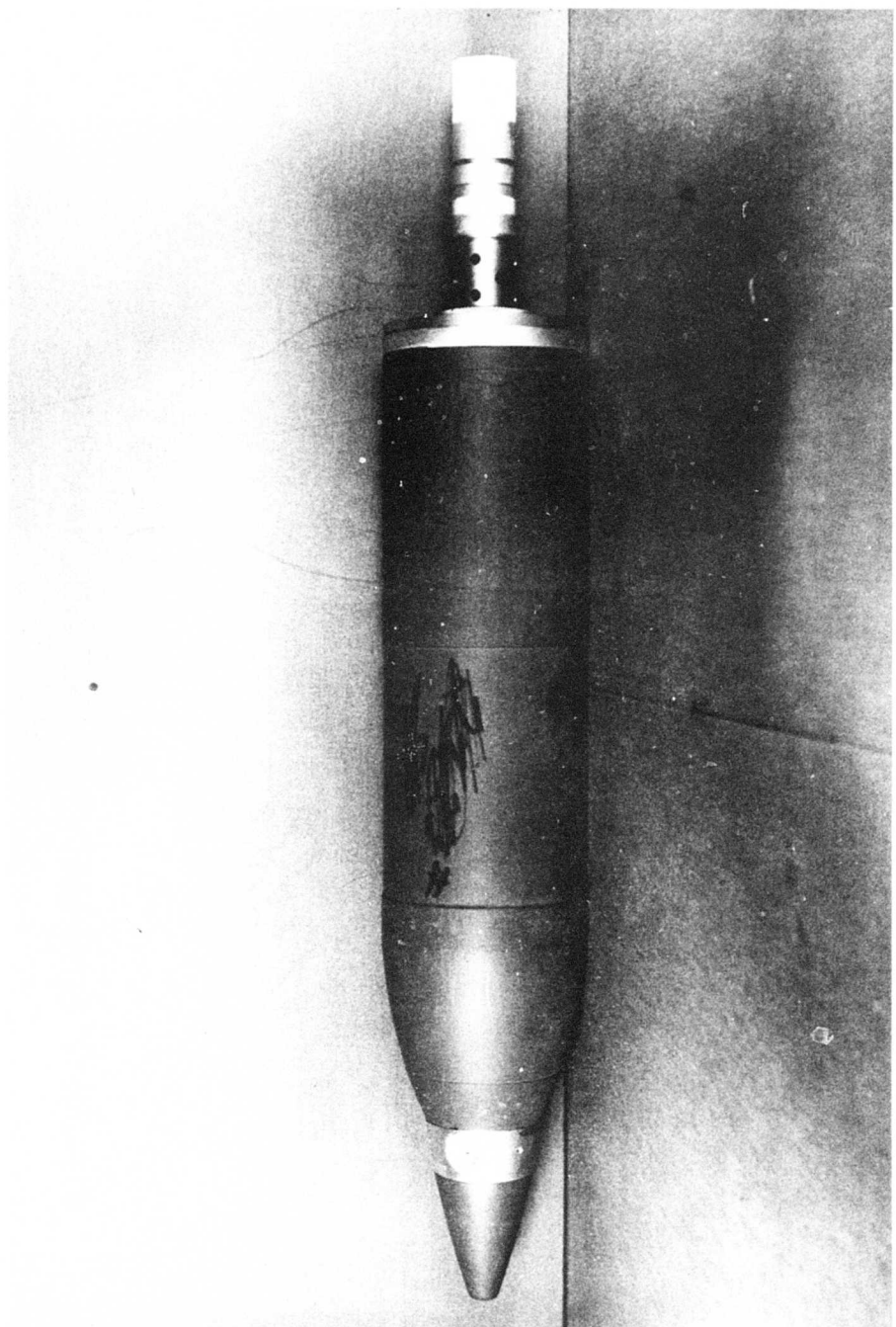


Figure 6. A Yawsonde Instrumented 107mm Mortar Shell

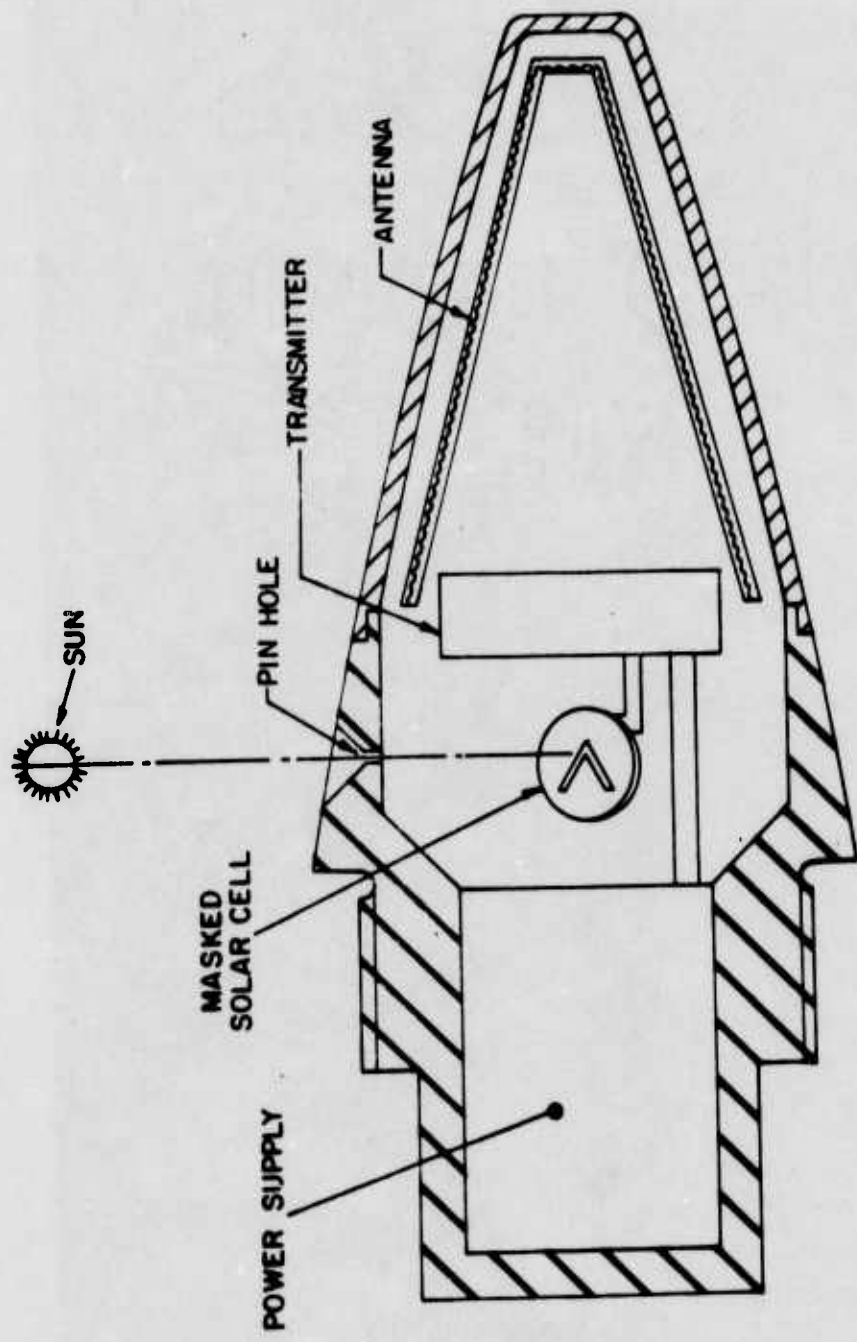


FIGURE 7 SCHEMATIC OF THE HDL YAWSONDE

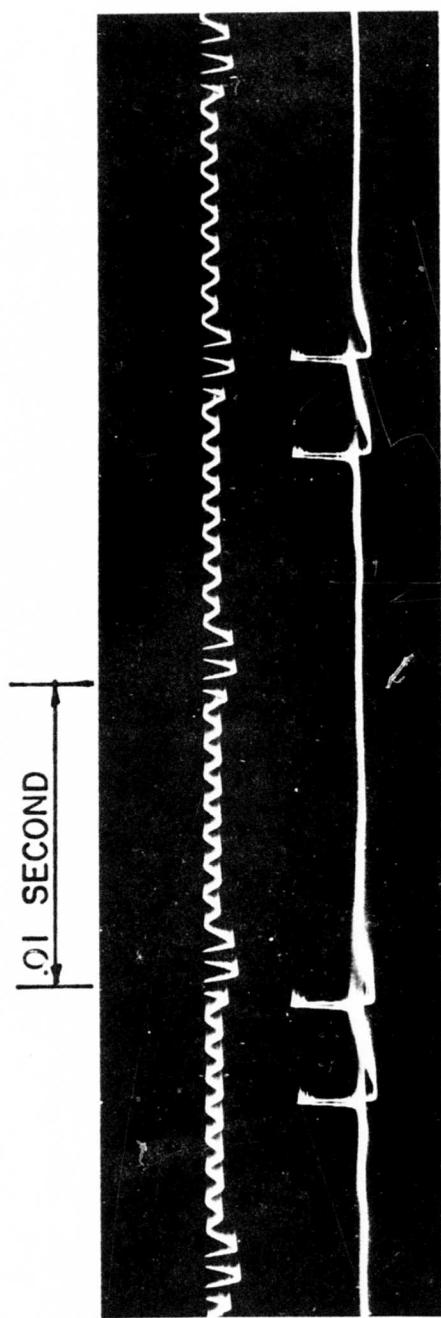


FIGURE 8 REPRODUCTION OF A TELEMETRY PULSE TRAIN

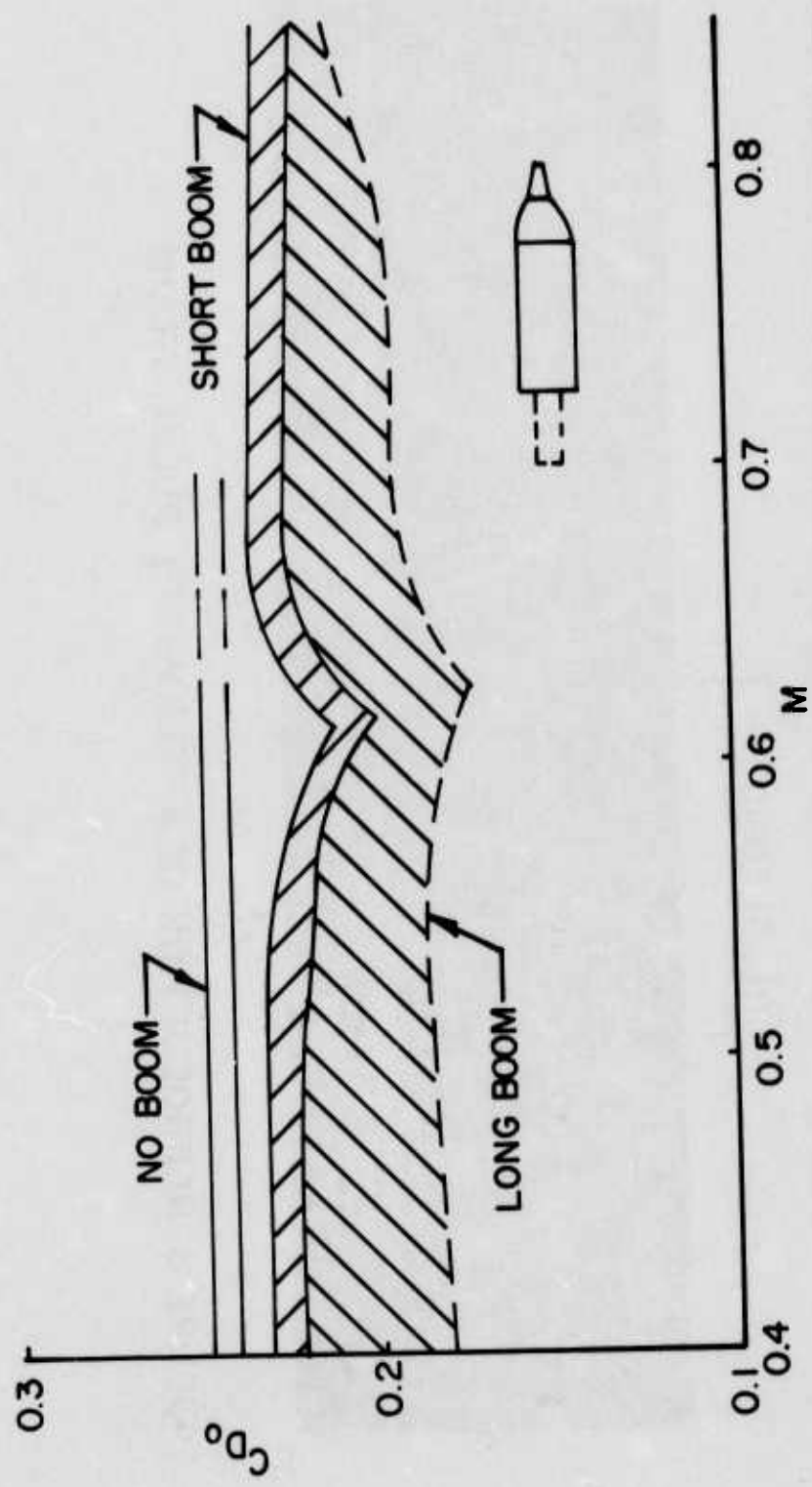


FIGURE 9 DRAG COEFFICIENT vs MACH NUMBER FOR A SQUARE-BASED SHELL WITH DIFFERENT BOOM LENGTHS

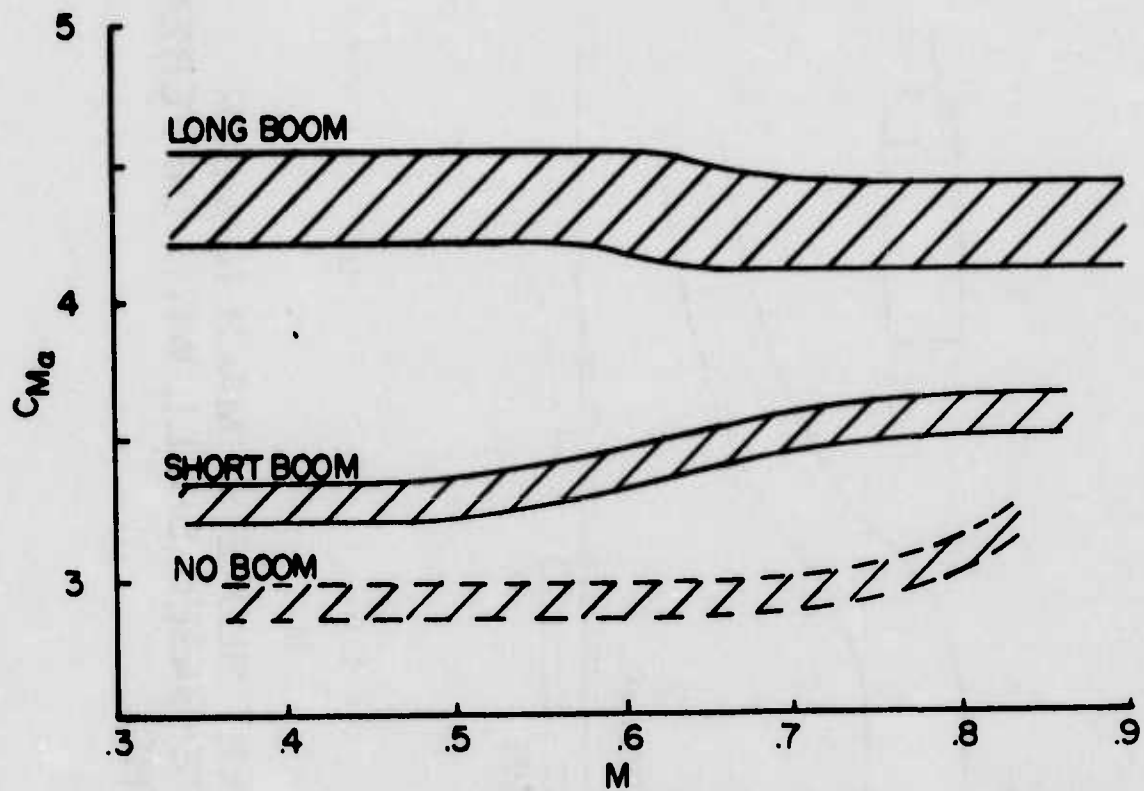


FIGURE 10 STATIC MOMENT SLOPE vs MACH NUMBER
FOR VARIOUS TEST MODELS

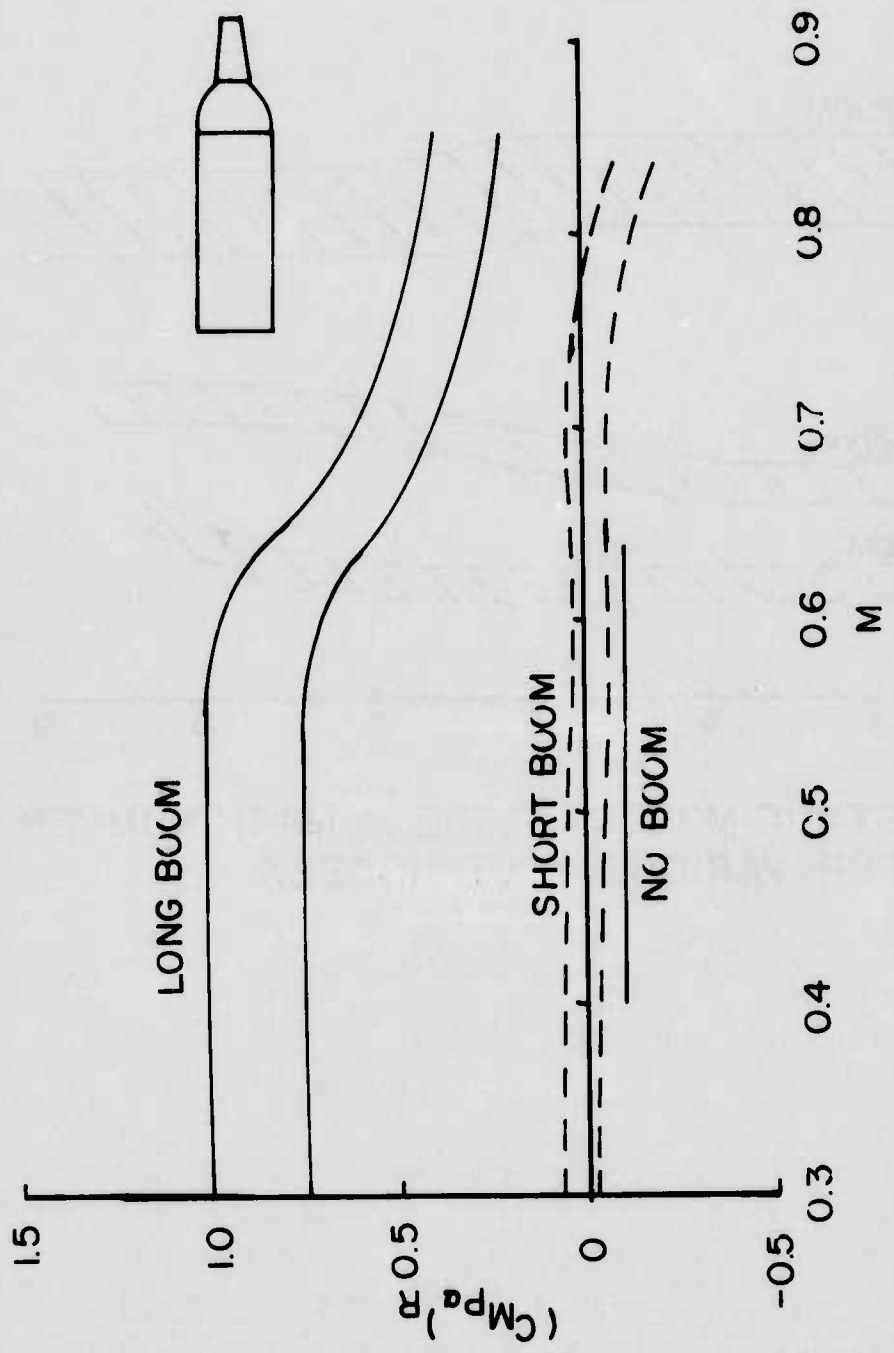


FIGURE II MAGNUS MOMENT SLOPE vs MACH NUMBER
FOR A SQUARE-BASED SHELL WITH DIFFERENT
BOOM LENGTHS

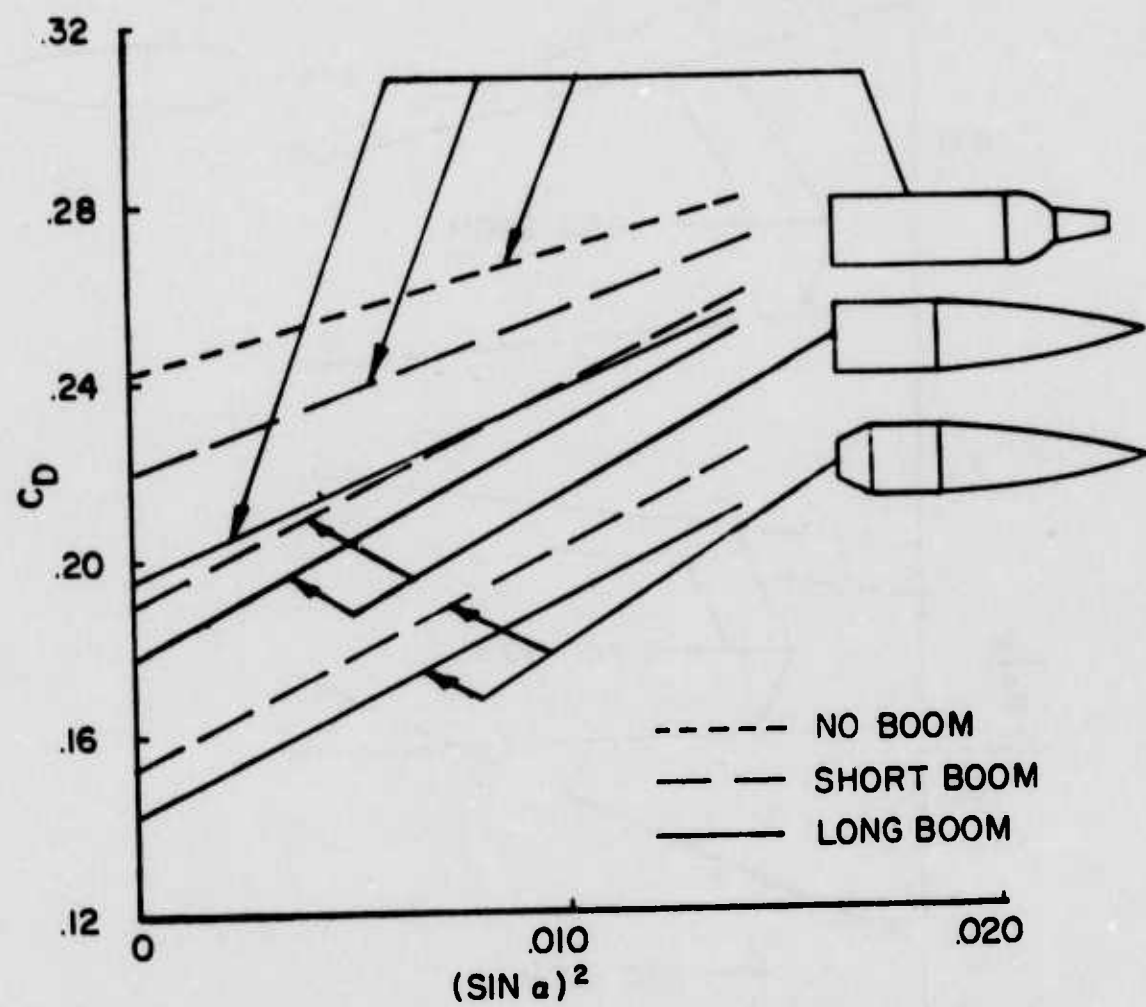


FIGURE 12 DRAG COEFFICIENT vs YAW SQUARED FOR VARIOUS TEST MODELS

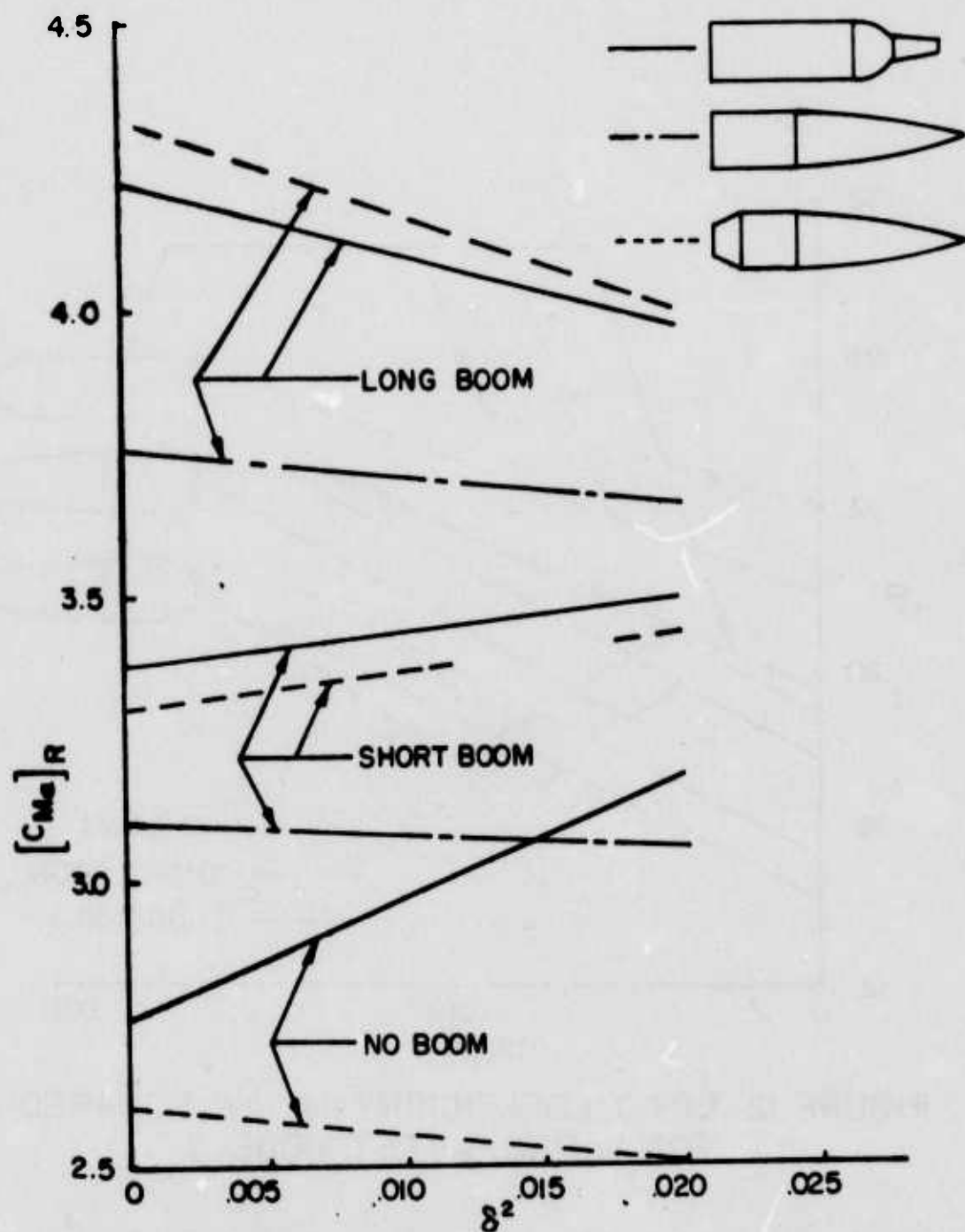


FIGURE 13 STATIC MOMENT SLOPE vs YAW SQUARED FOR VARIOUS TEST MODELS

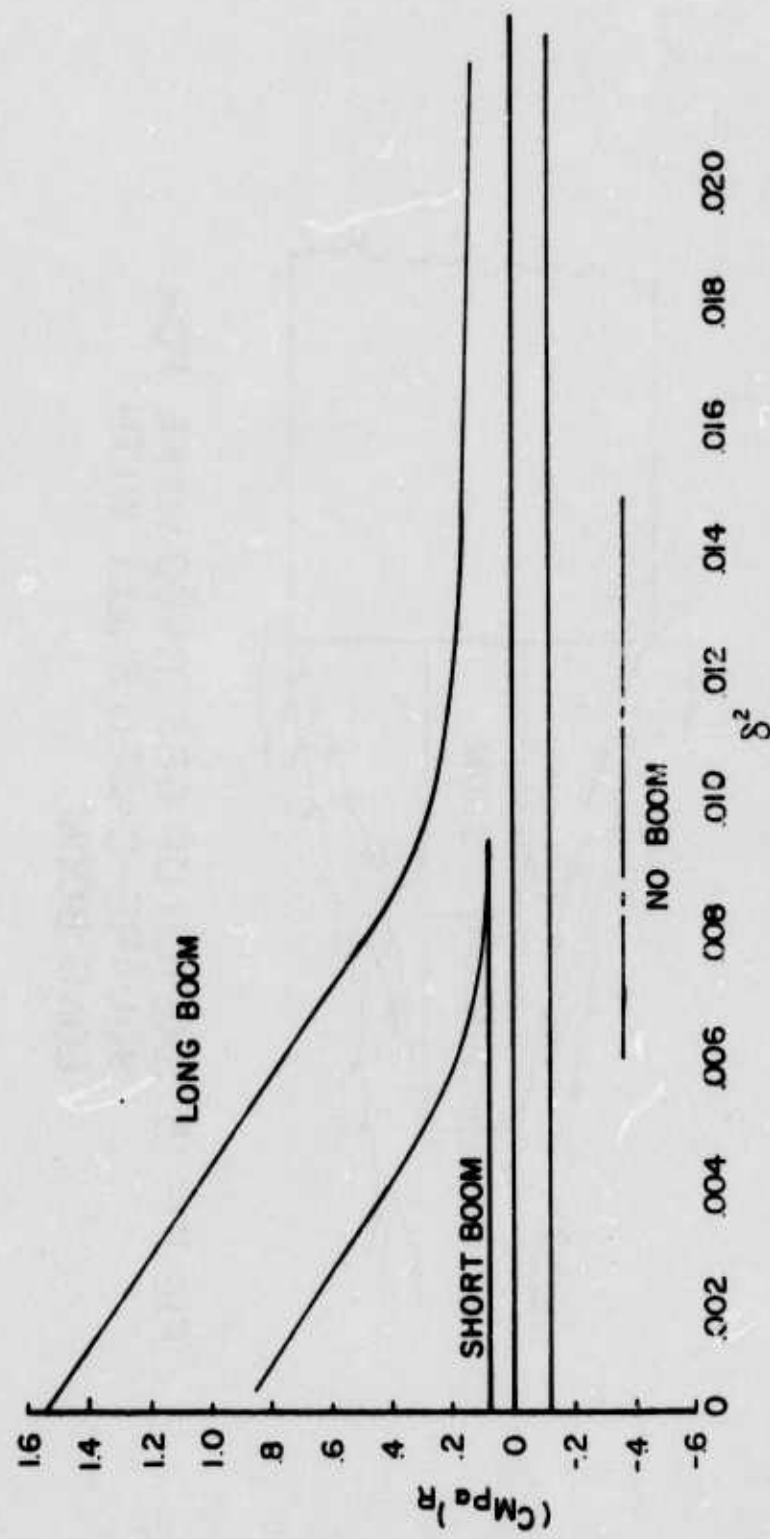


FIGURE I4 MAGNUS MOMENT SLOPE vs δ^2 FOR VARIOUS TEST MODELS

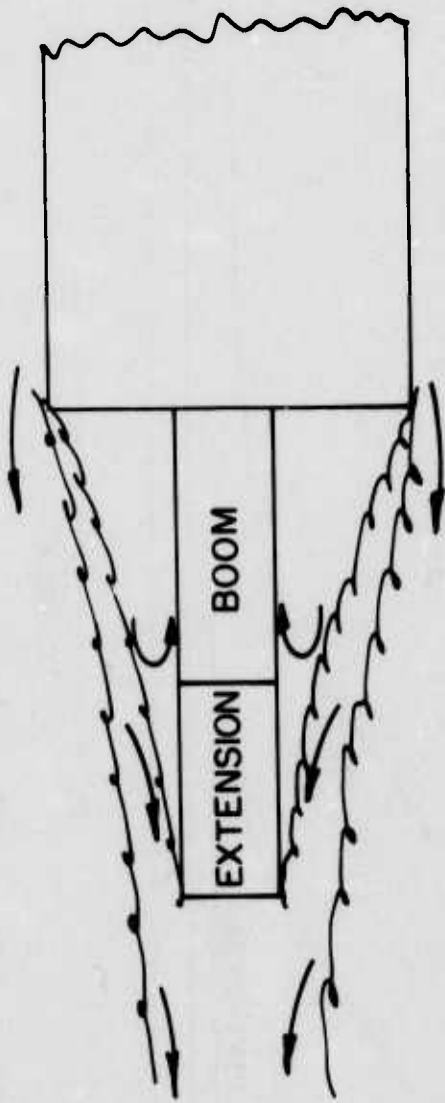


FIGURE 15 SKETCH OF OBSERVED WAKE FOR
SQUARE-BASED SHELL WITH
LONG BOOM

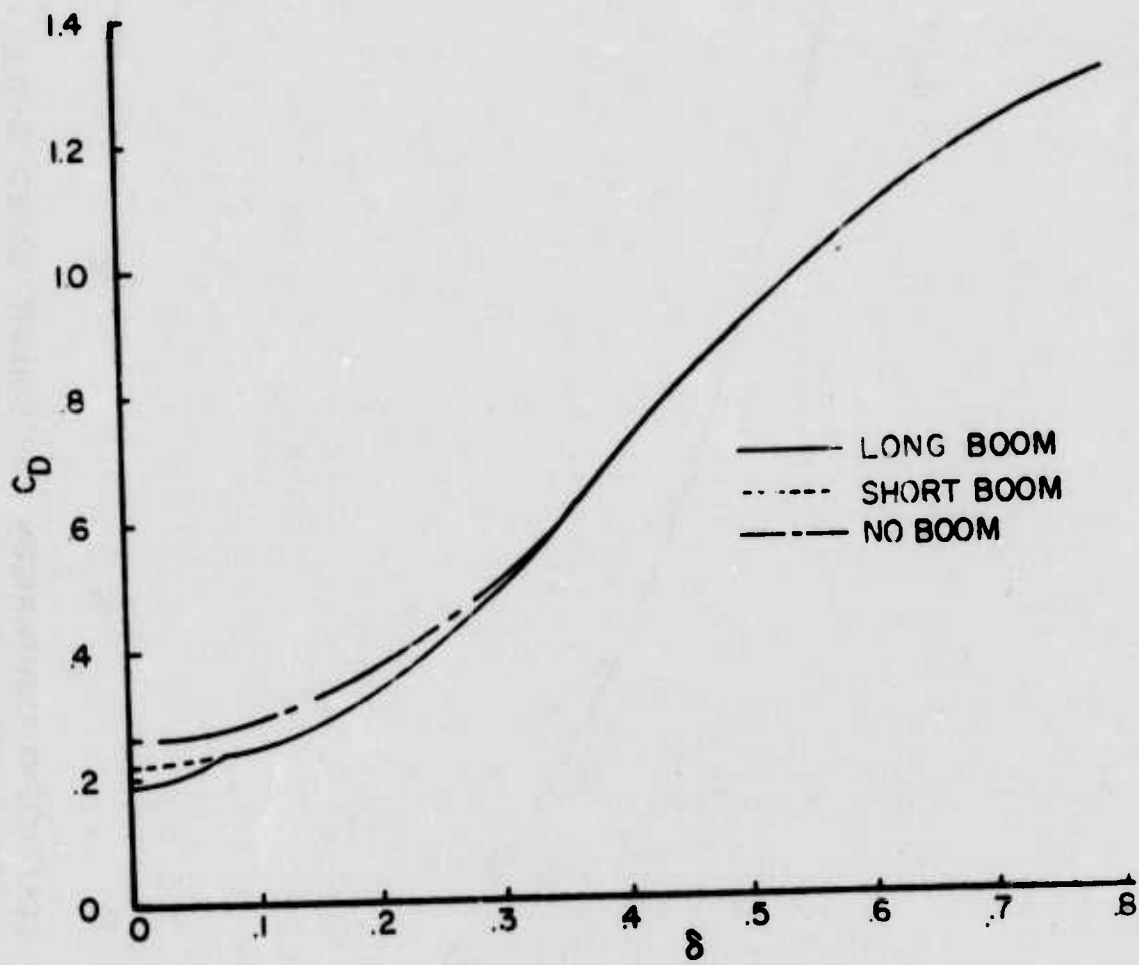


FIGURE 16 DRAG COEFFICIENT vs YAW FOR
SQUARE-BASED SHELL

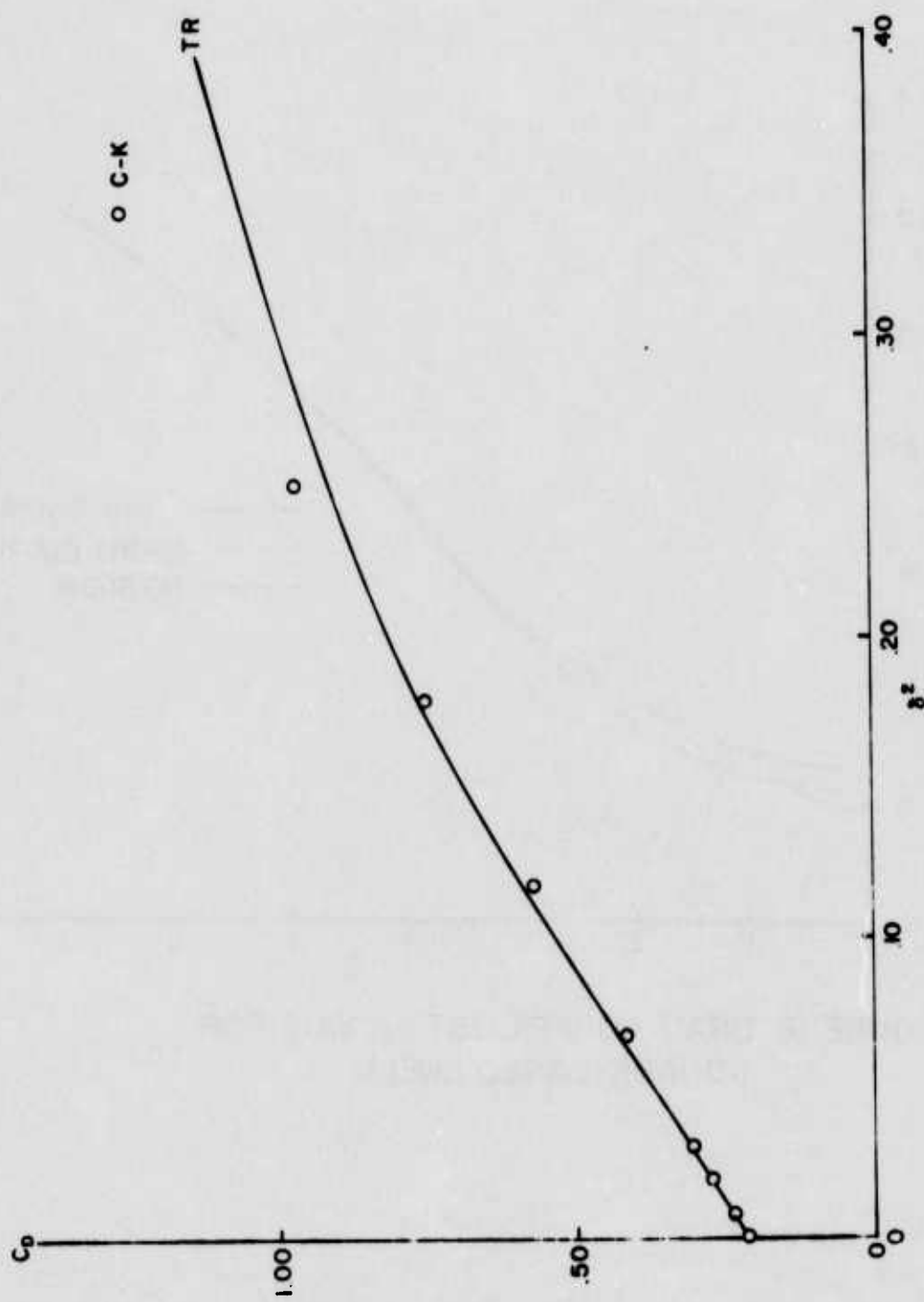


FIGURE 17 DRAG COEFFICIENT COMPARISON FOR SQUARE-BASED SHELL WITH SHORT BOOM

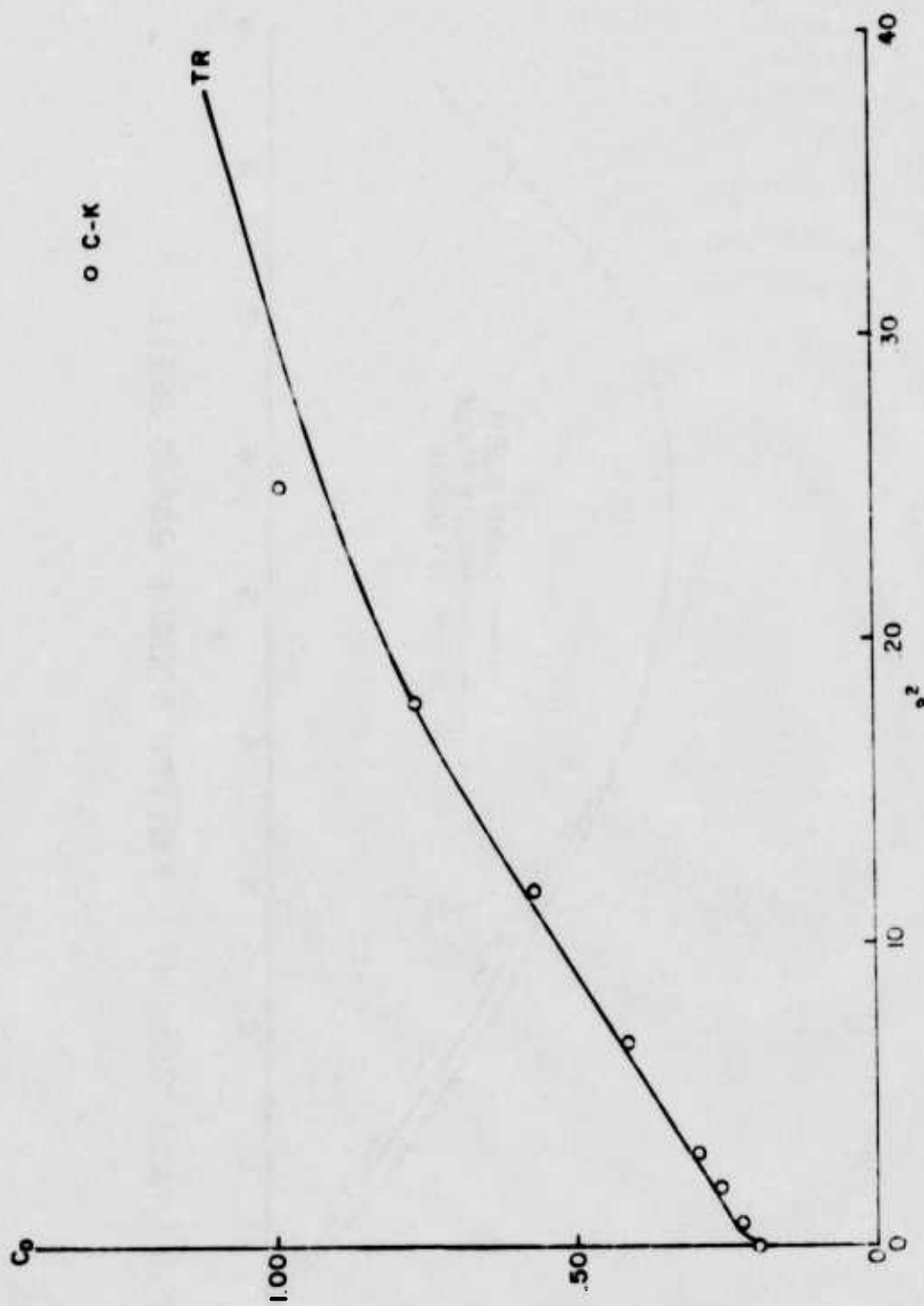


FIGURE 18 DRAG COEFFICIENT COMPARISON FOR SQUARE-BASED SHELL WITH LONG BOOM

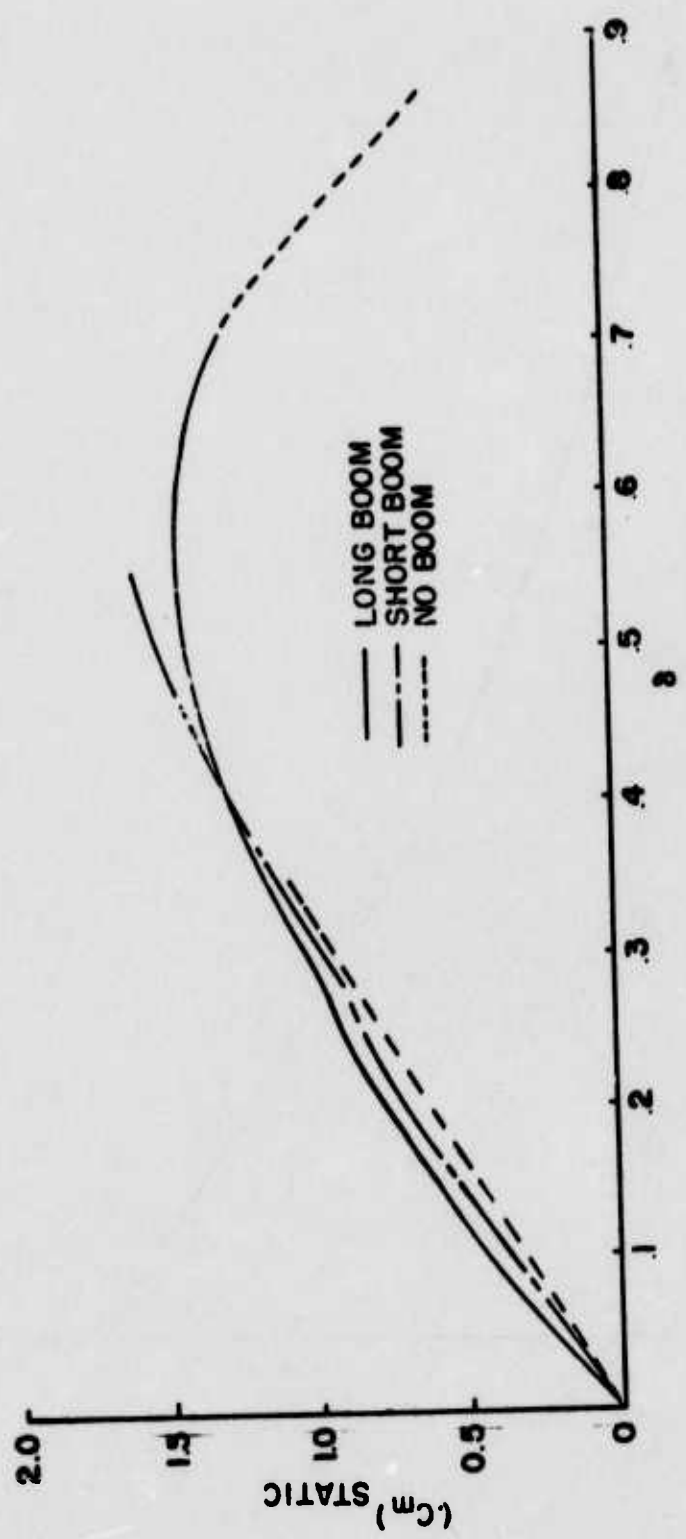


FIGURE 19 STATIC MOMENT vs YAW FOR SQUARE-BASED SHELL

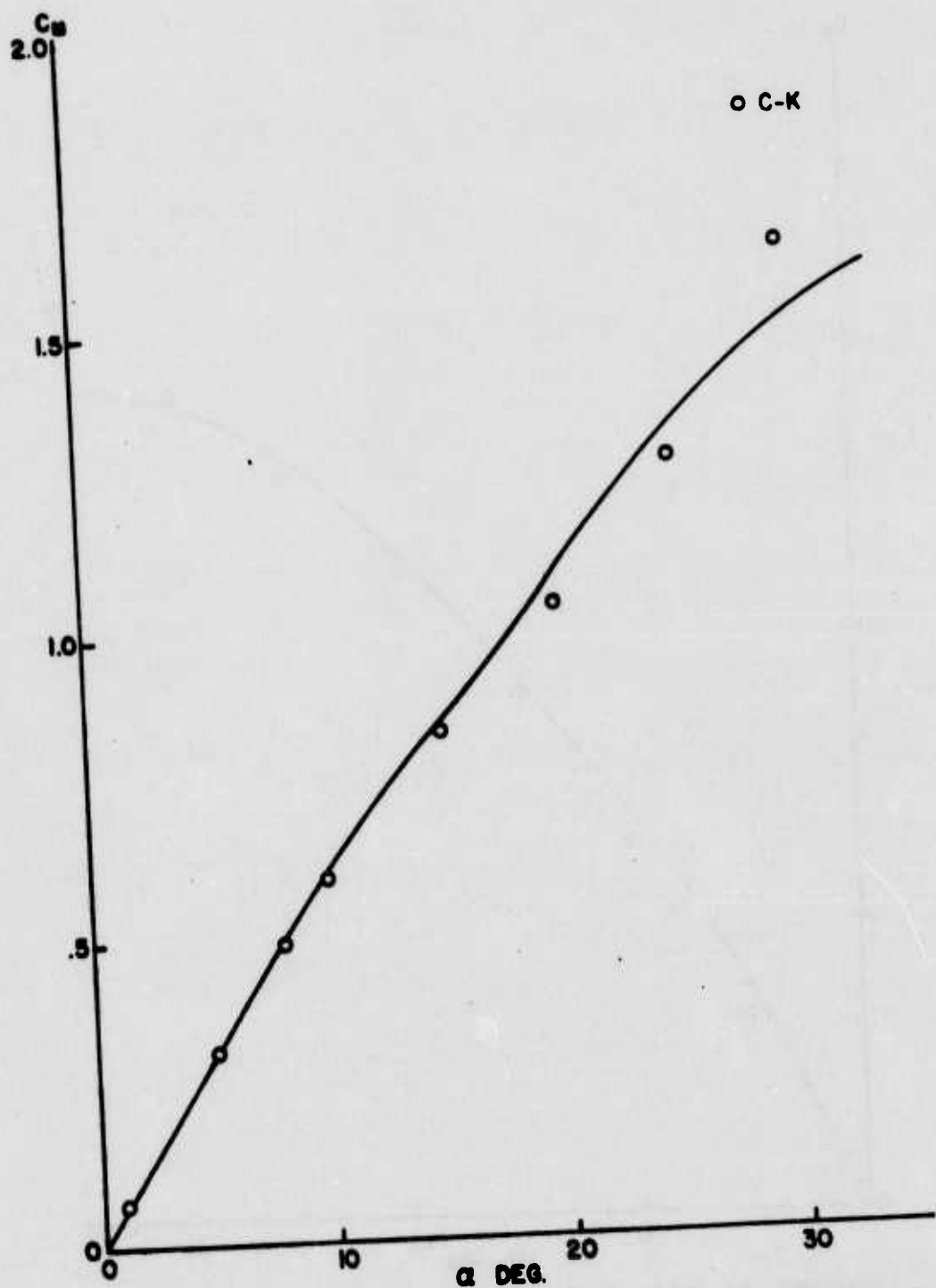


FIGURE 20 STATIC MOMENT COEFFICIENT COMPARISON
FOR SQUARE-BASED SHELL WITH SHORT BOOM

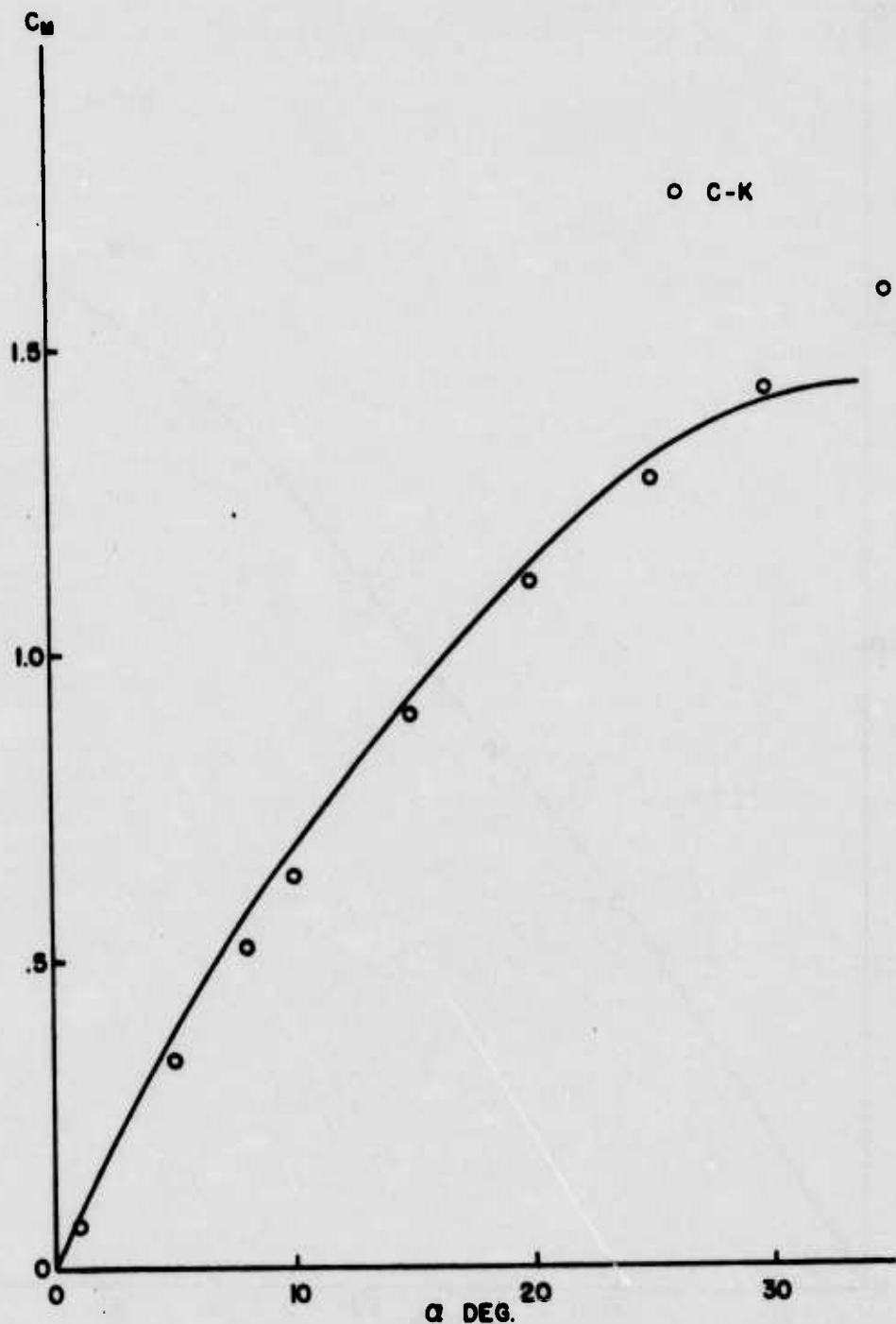


FIGURE 21 STATIC MOMENT COEFFICIENT COMPARISON
FOR SQUARE-BASED SHELL WITH LONG BOOM

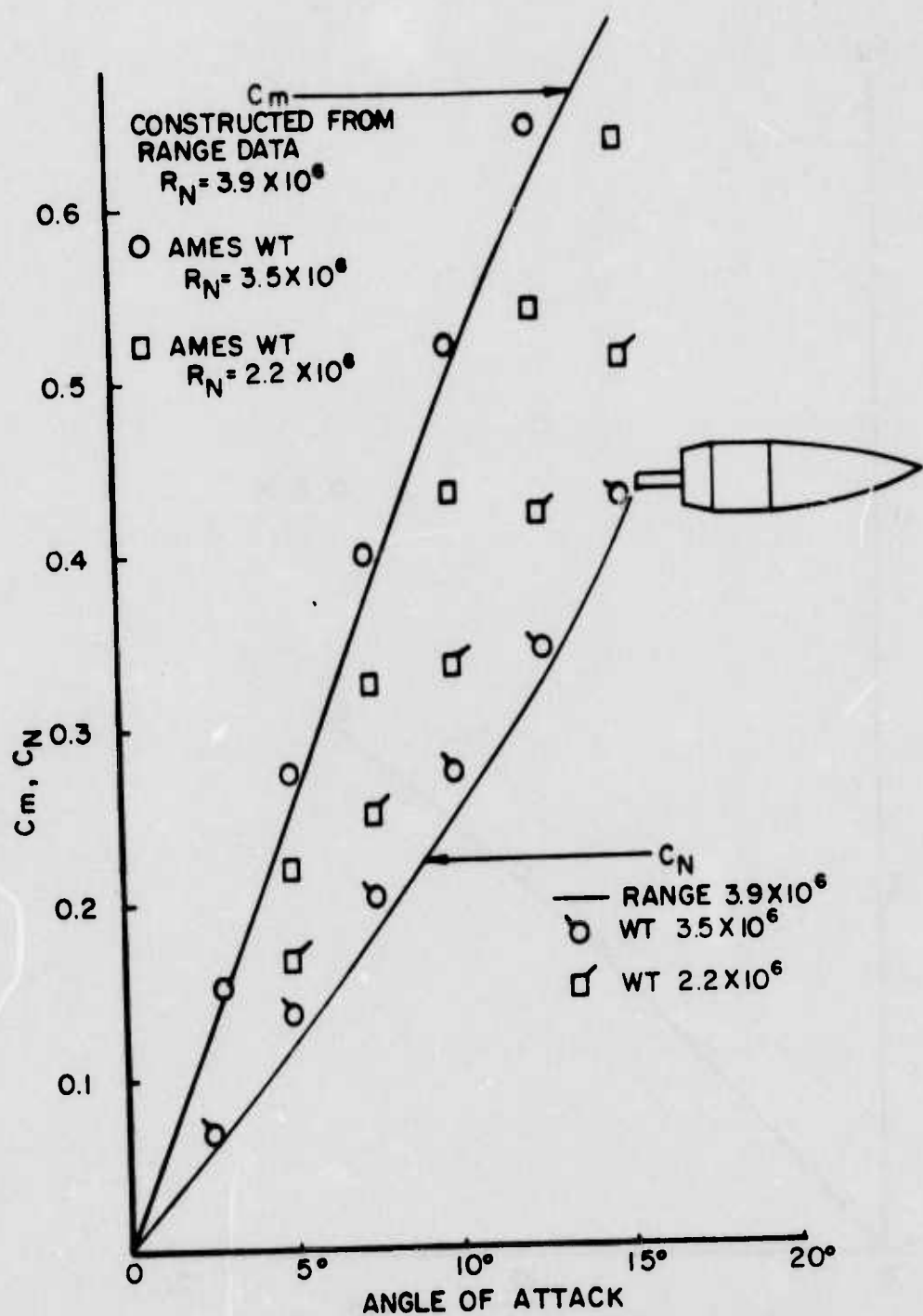


FIGURE 22 STATIC MOMENT AND NORMAL FORCE COEFFICIENTS vs YAW FOR BOAT-TAILED SHELL

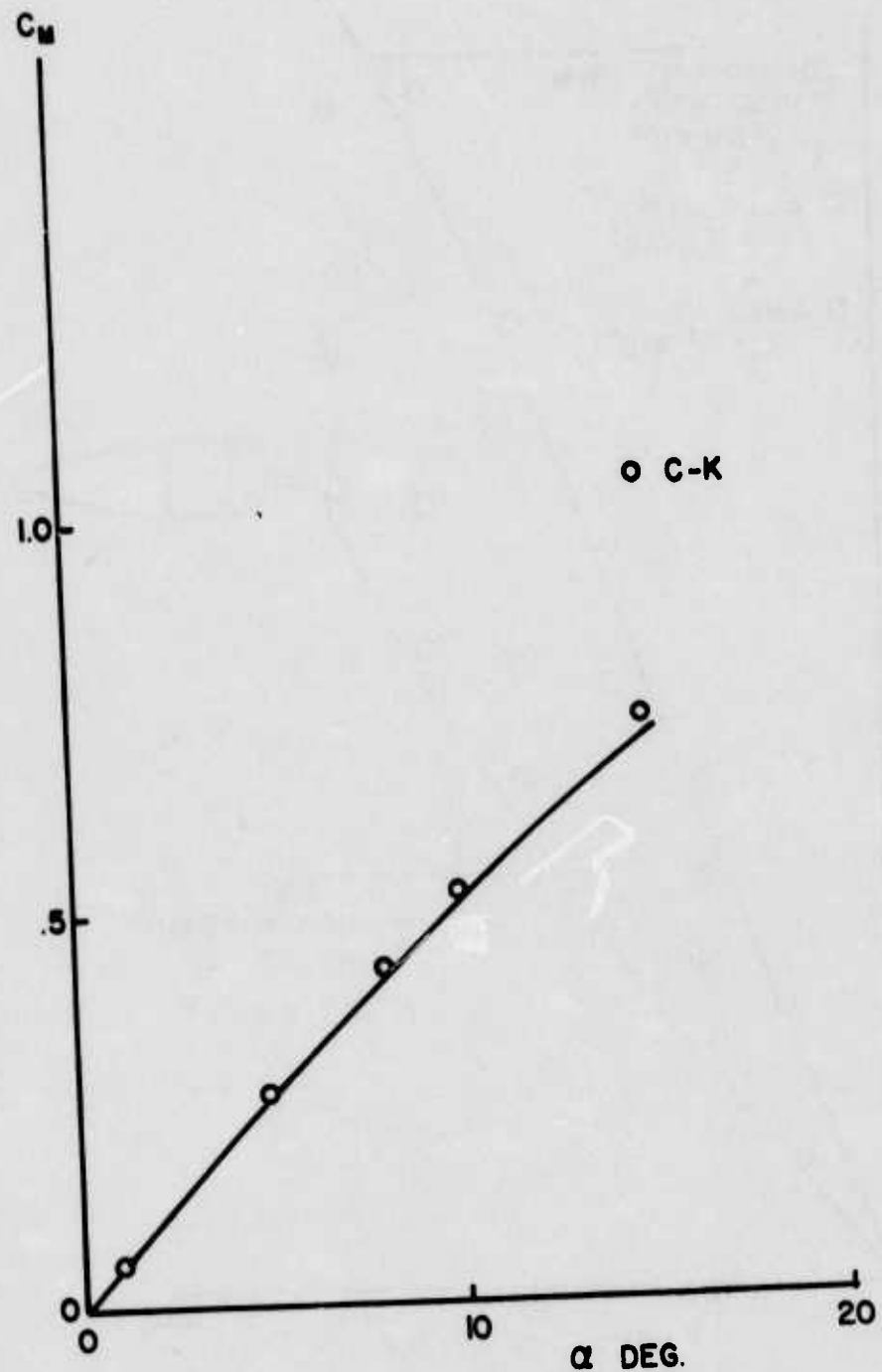


FIGURE 23 STATIC MOMENT COEFFICIENT COMPARISON
FOR BOATTAILED SHELL

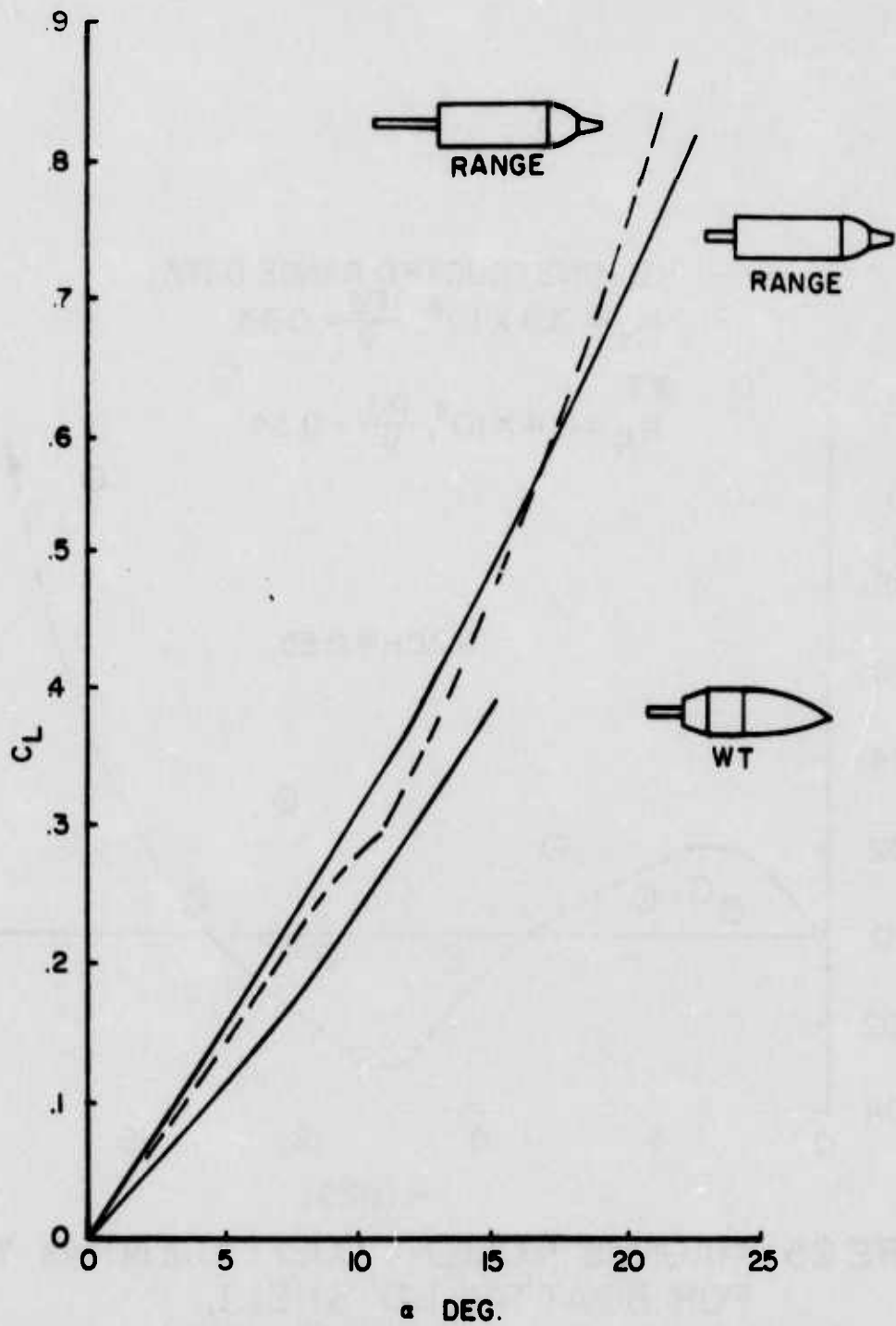


FIGURE 24 LIFT COEFFICIENT vs YAW FOR VARIOUS TEST MODELS

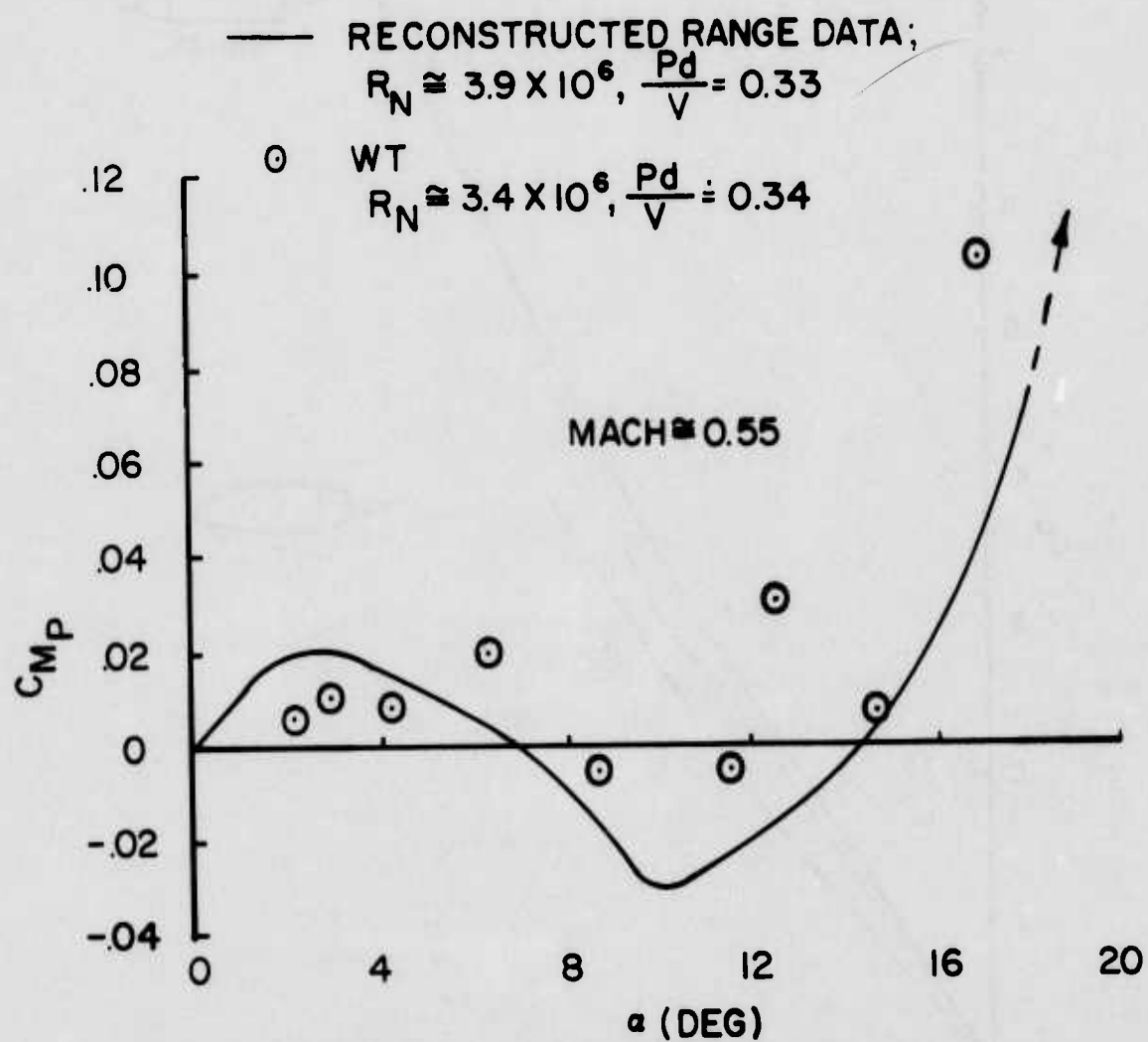


FIGURE 25 MAGNUS MOMENT COEFFICIENT vs YAW FOR BOATTAILED SHELL

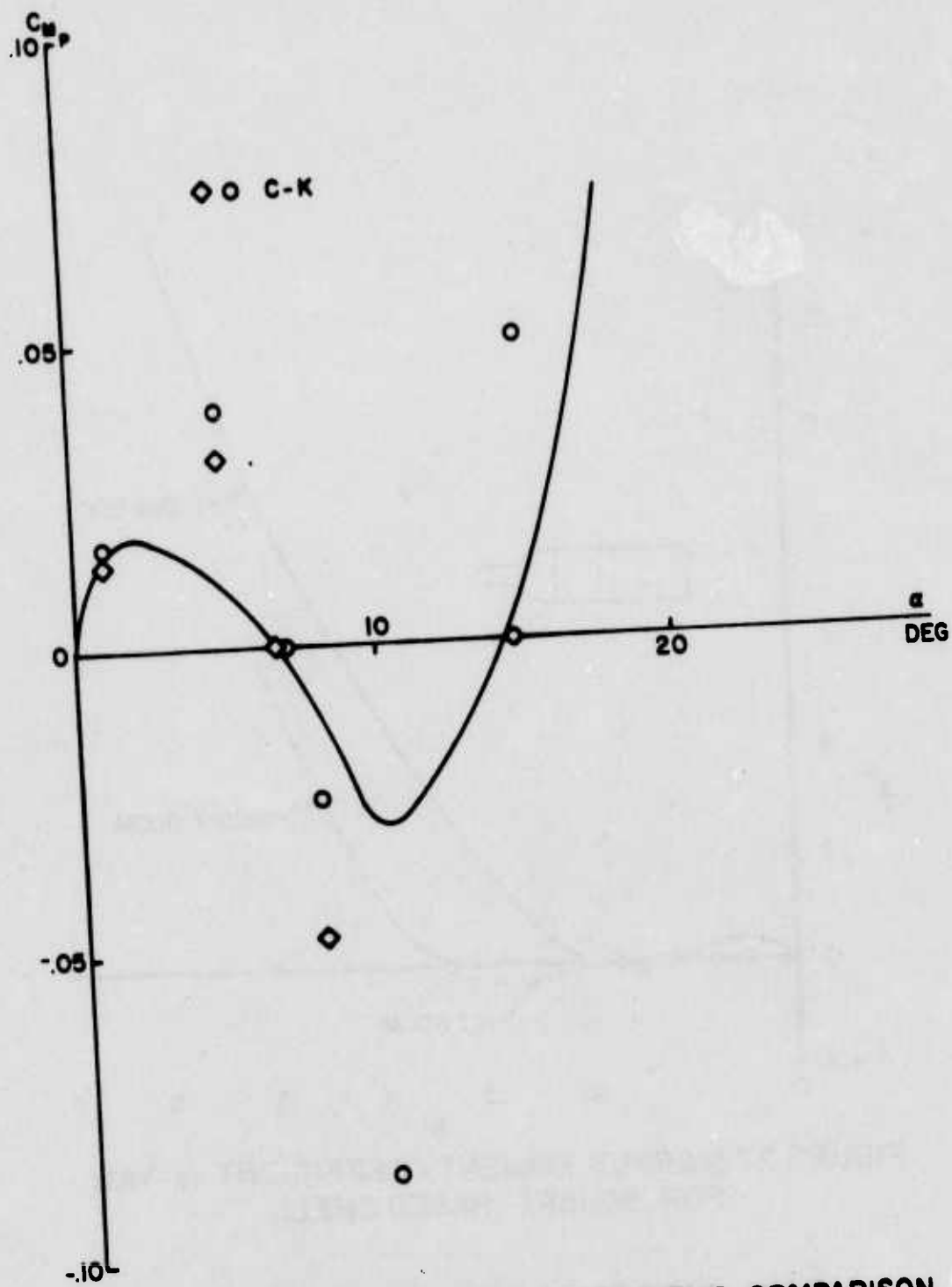


FIGURE 26 MAGNUS MOMENT COEFFICIENT COMPARISON
FOR BOATTAILED SHELL

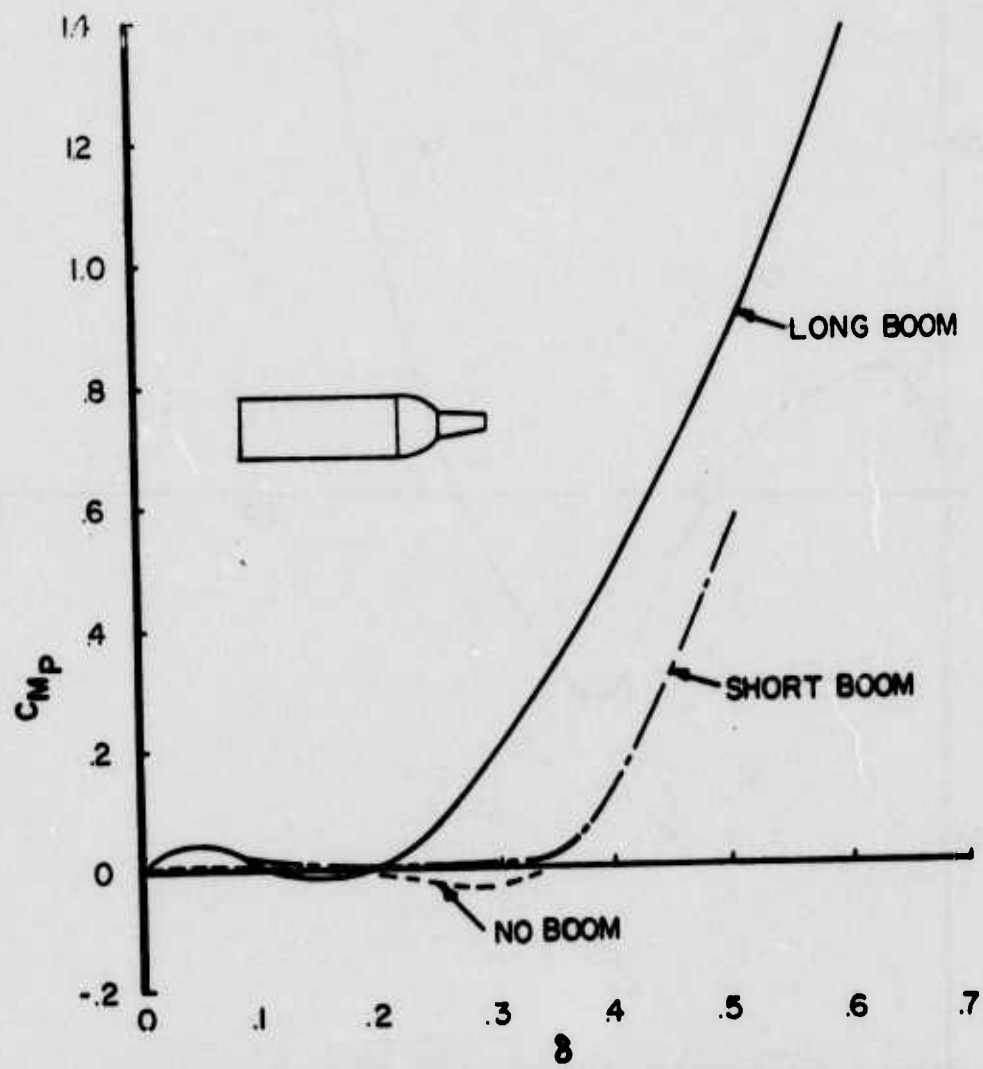
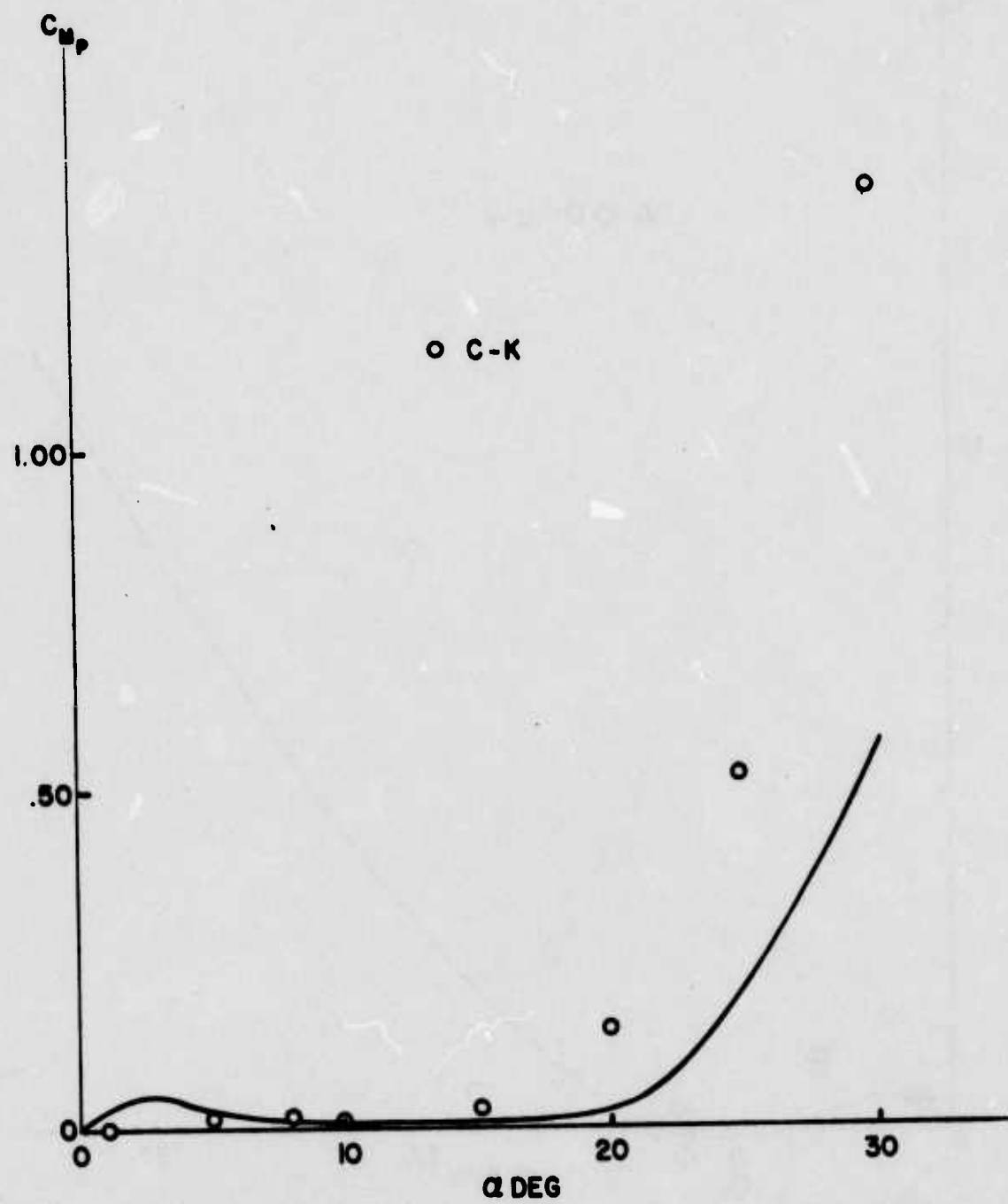


FIGURE 27 MAGNUS MOMENT COEFFICIENT vs YAW
FOR SQUARE-BASED SHELL



**FIGURE 28 MAGNUS MOMENT COEFFICIENT COMPARISON
FOR SQUARE-BASED SHELL WITH SHORT BOOM**

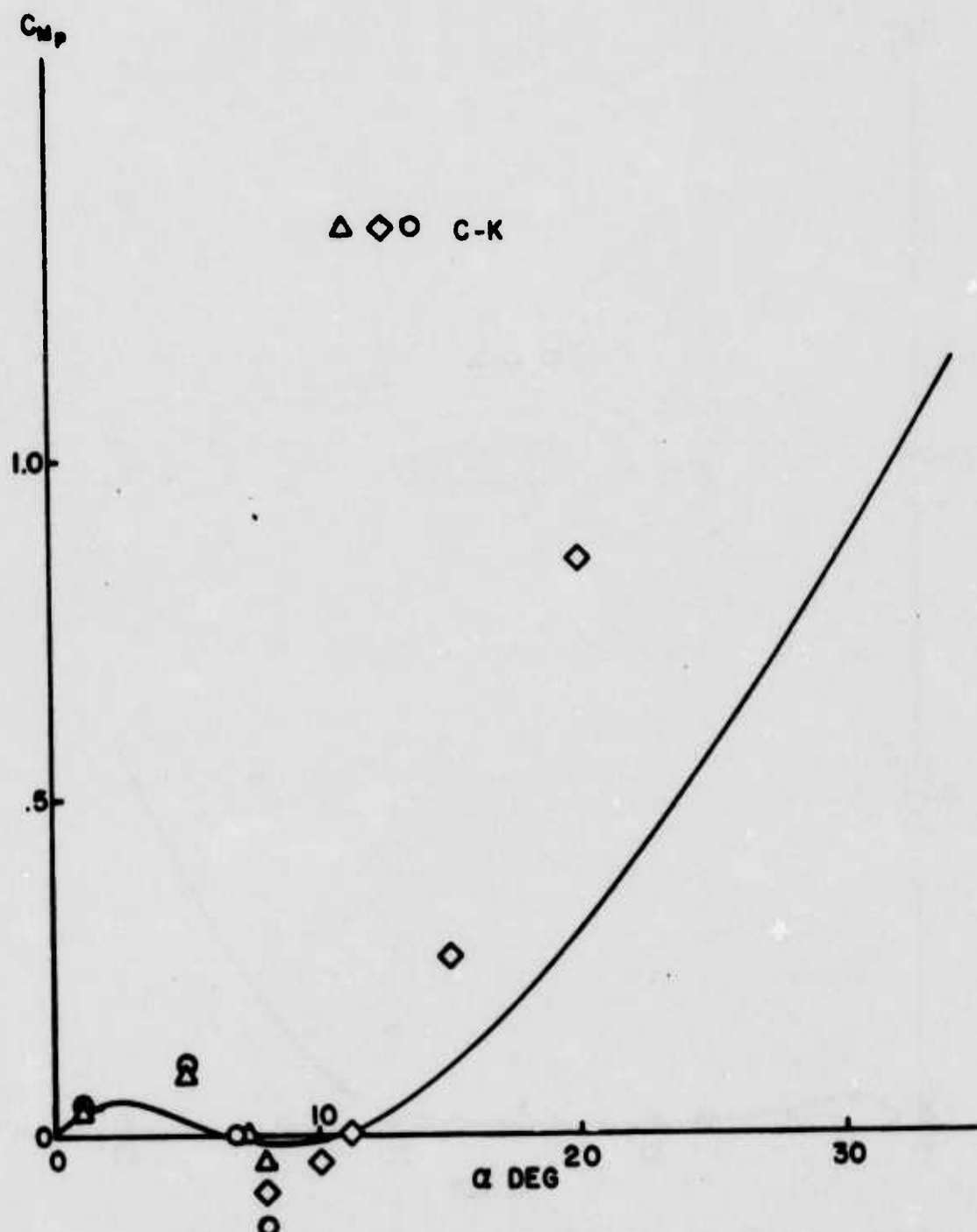


FIGURE 29 MAGNUS MOMENT COEFFICIENT COMPARISON
FOR SQUARE-BASED SHELL WITH LONG BOOM

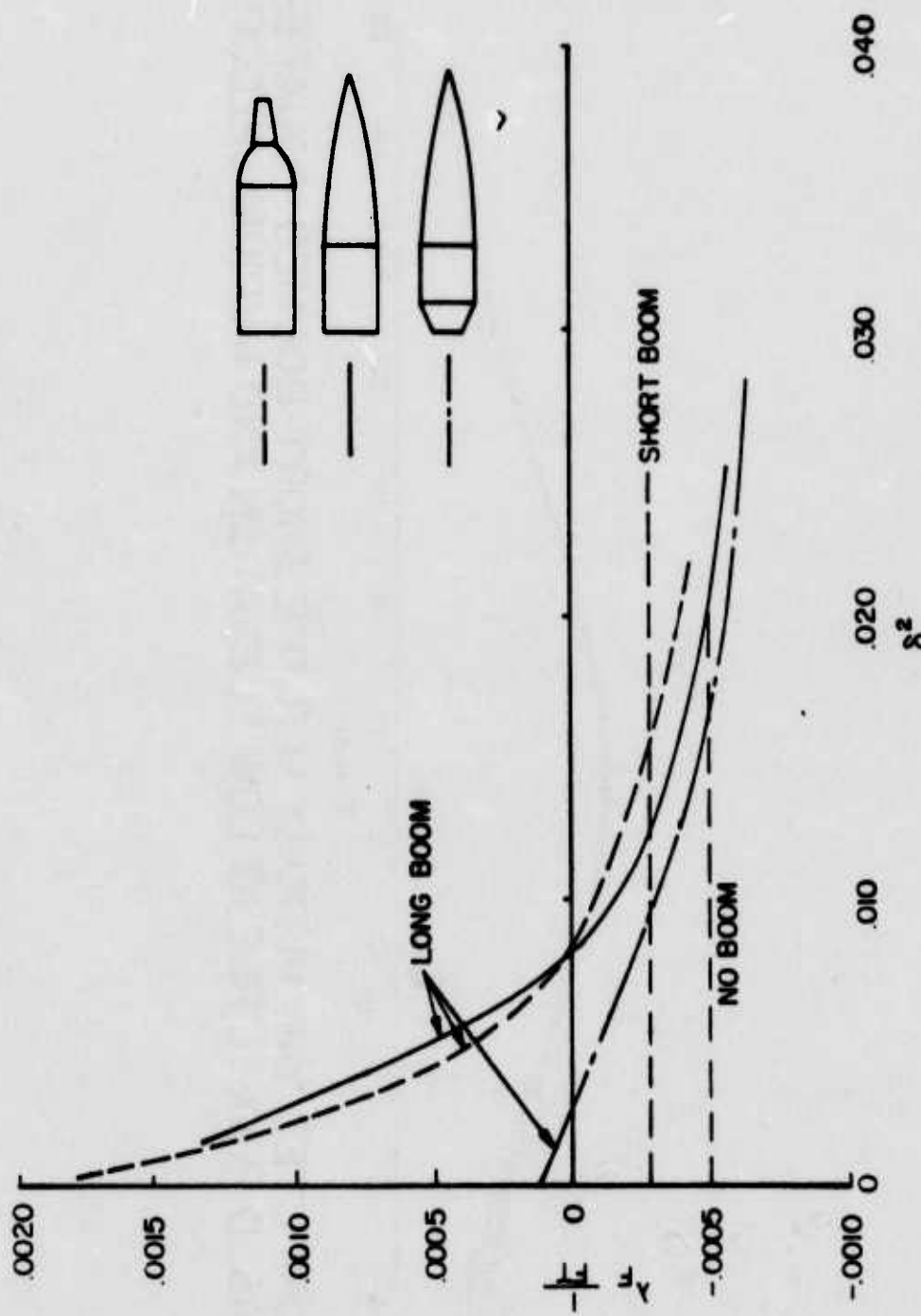


FIGURE 30 DAMPING FACTOR vs. δ^2 FOR VARIOUS TEST MODELS

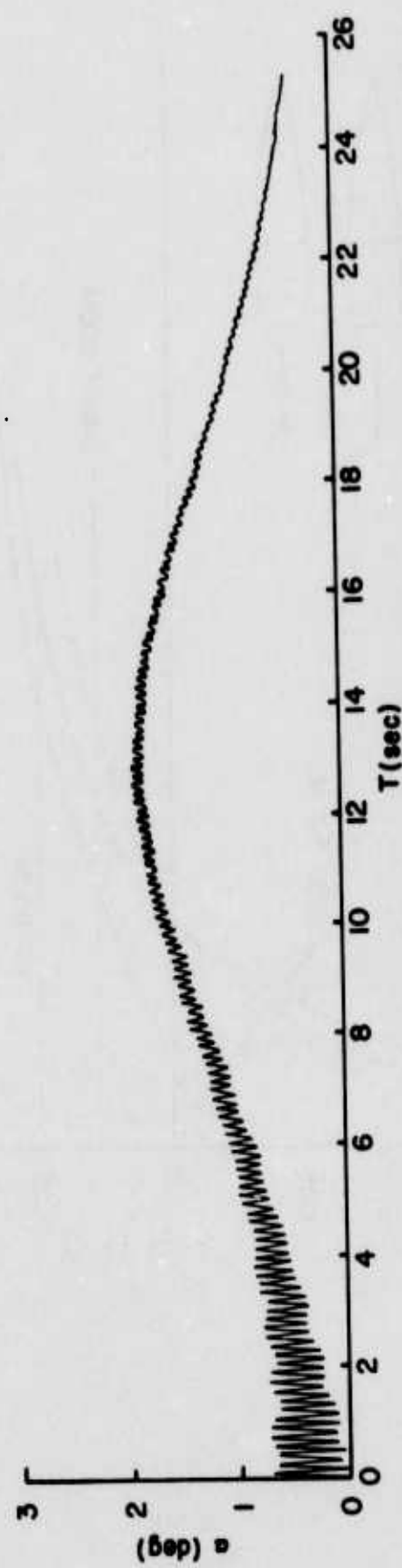


FIGURE 3I COMPUTED YAW HISTORY FOR THE SHORT-BOOMED SQUARE-BASED PROJECTILE AT LOW ELEVATION AND MEDIUM VELOCITY

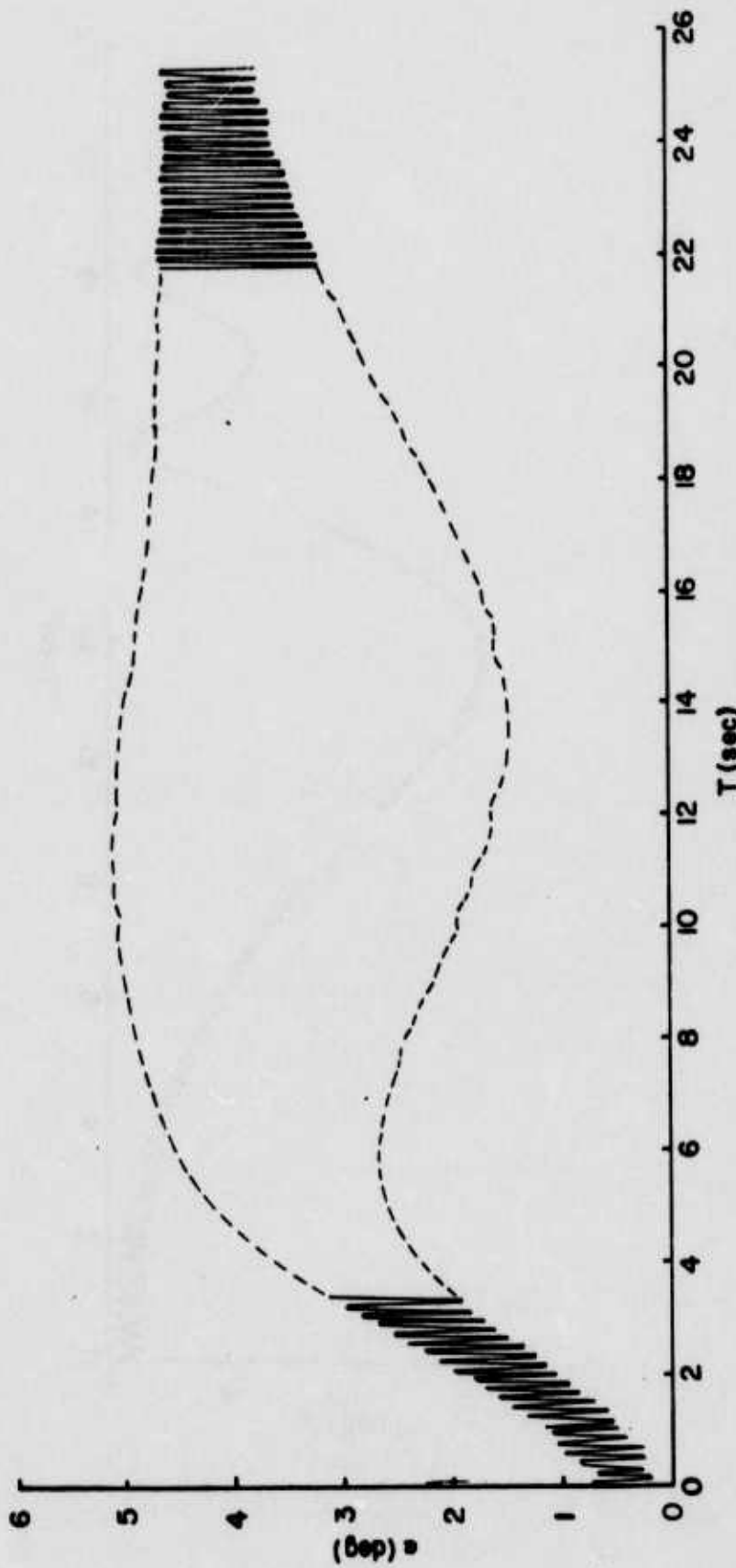


FIGURE 32 COMPUTED YAW HISTORY FOR THE LONG-BOOMED SQUARE-BASED PROJECTILE AT LOW ELEVATION AND MEDIUM VELOCITY

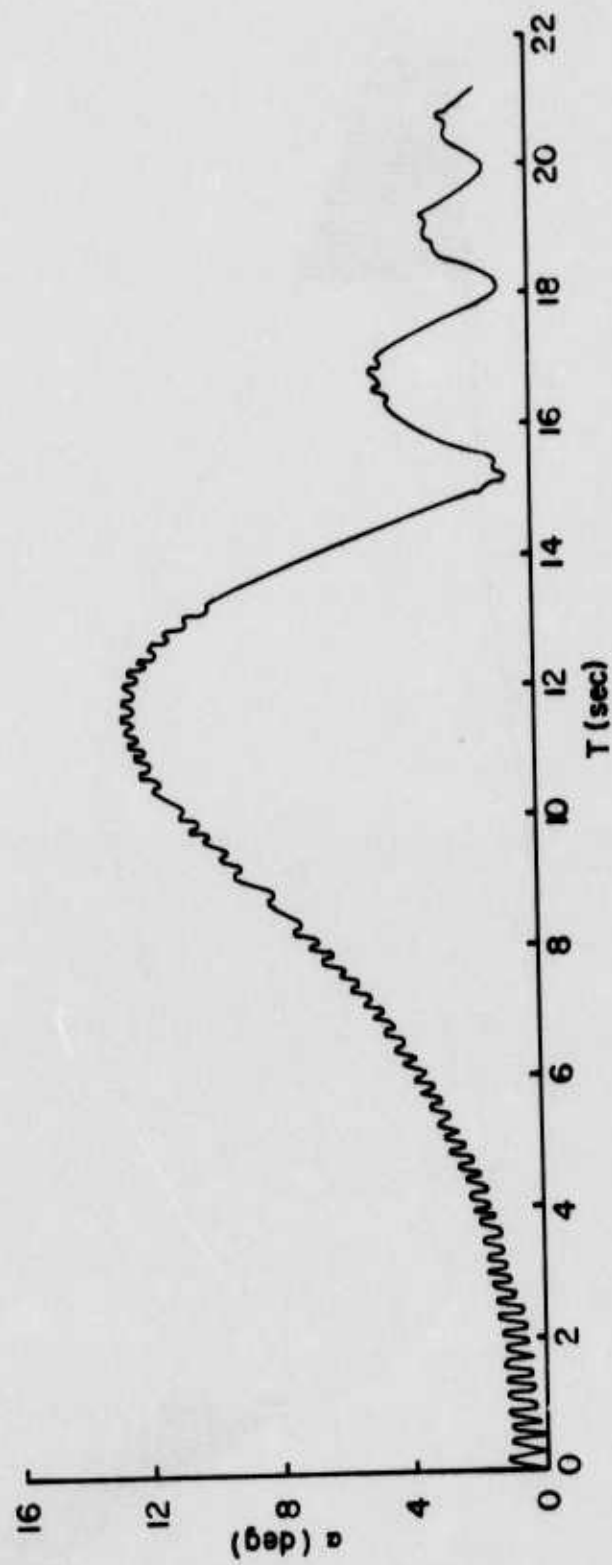


Figure 33. Computed Yaw History for the Short-Boomed Square-Based Projectile
at High Elevation and Low Velocity

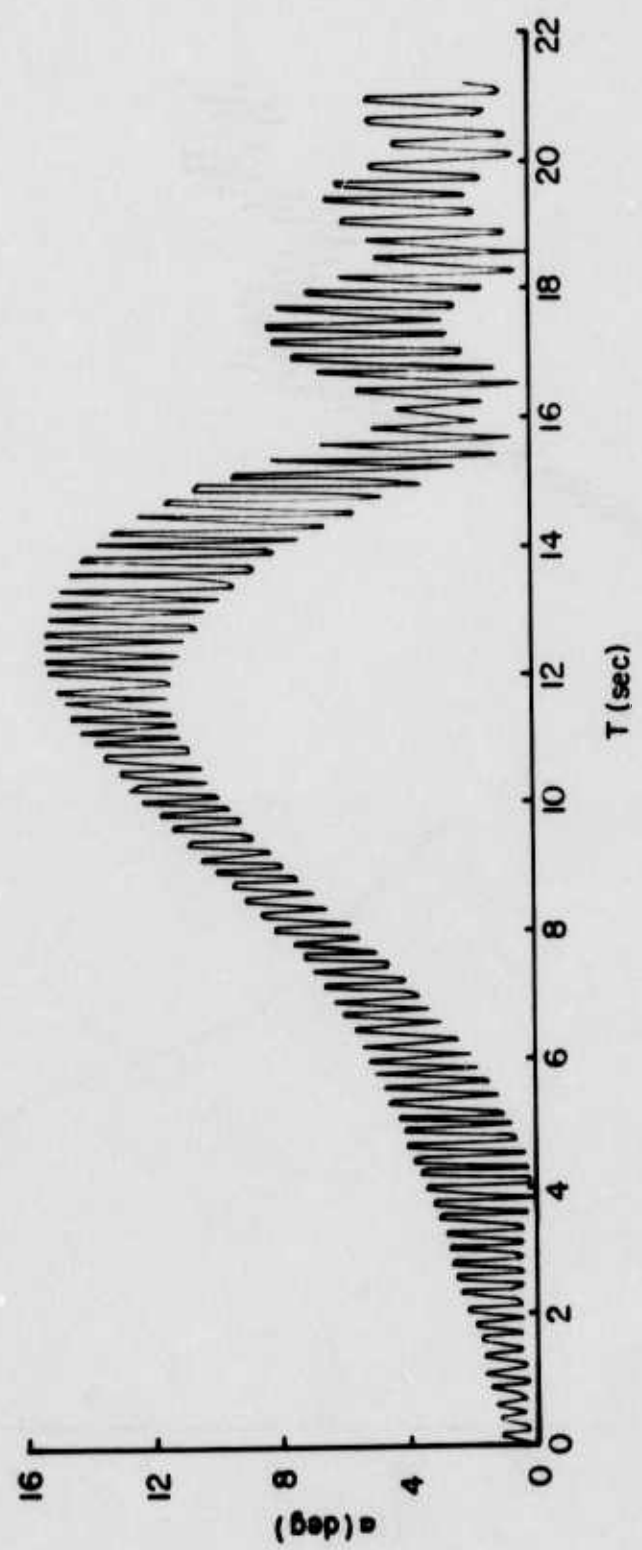


Figure 34. Computed Yaw History for the Long-Boomed Square-Based Projectile
at High Elevation and Low Velocity

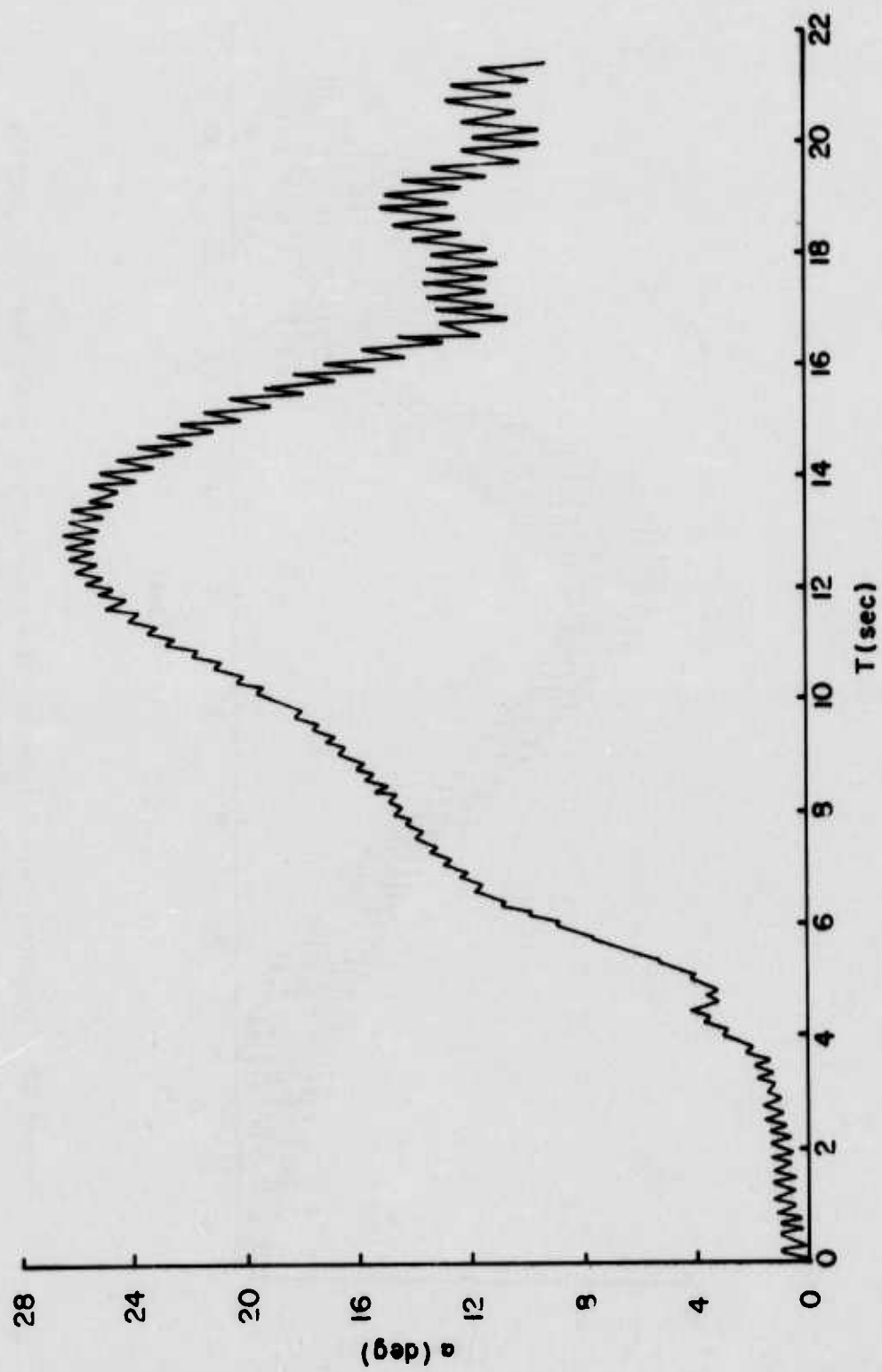


Figure 35. Computed Yaw History for the Short-Boomed Square-Based Projectile at High Elevation and Low Velocity with Wind Shear at the Summit

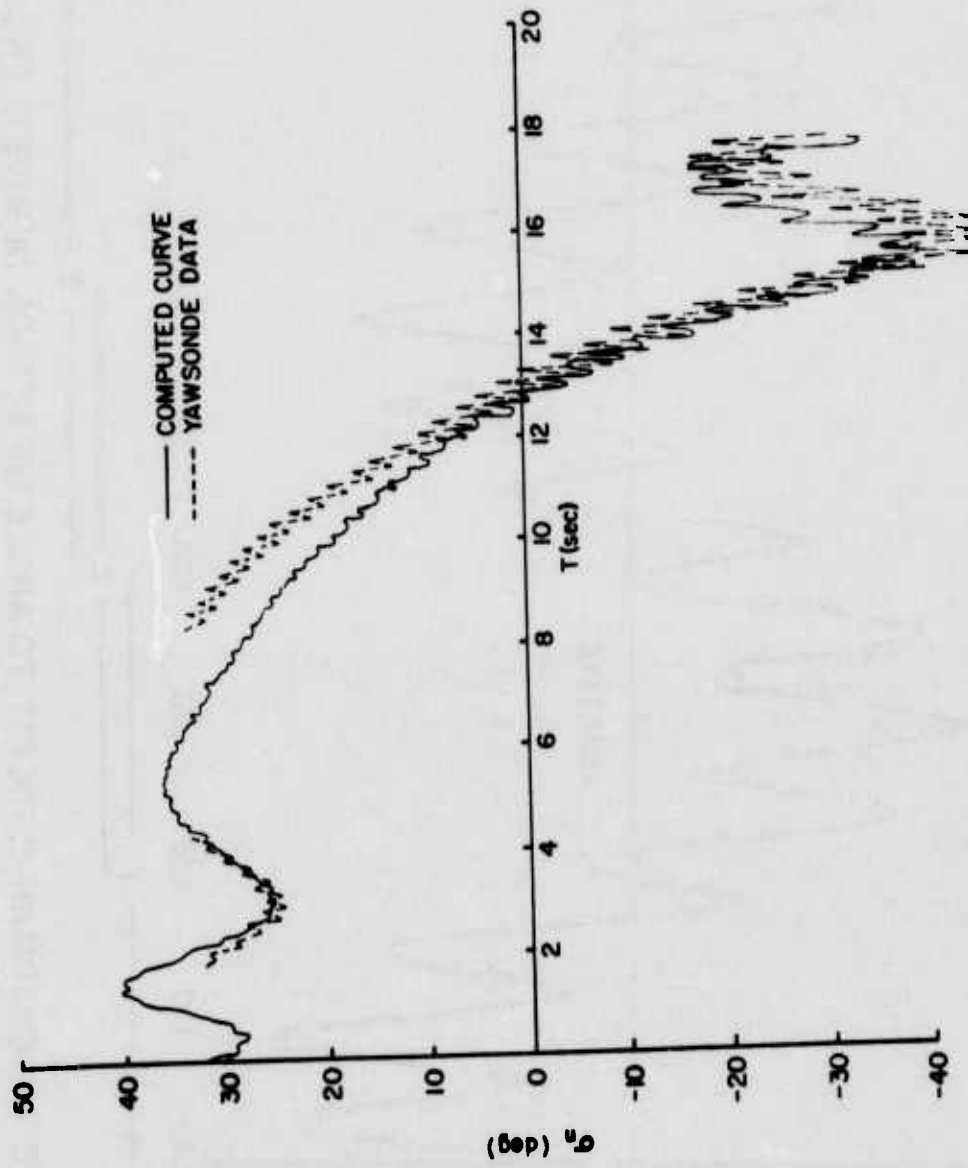


Figure 36. Comparison of the Computed Solar Aspect Angle History with the Yawsonde Data for the Short-Boomed Square-Based Projectile at High Elevation and Low Velocity

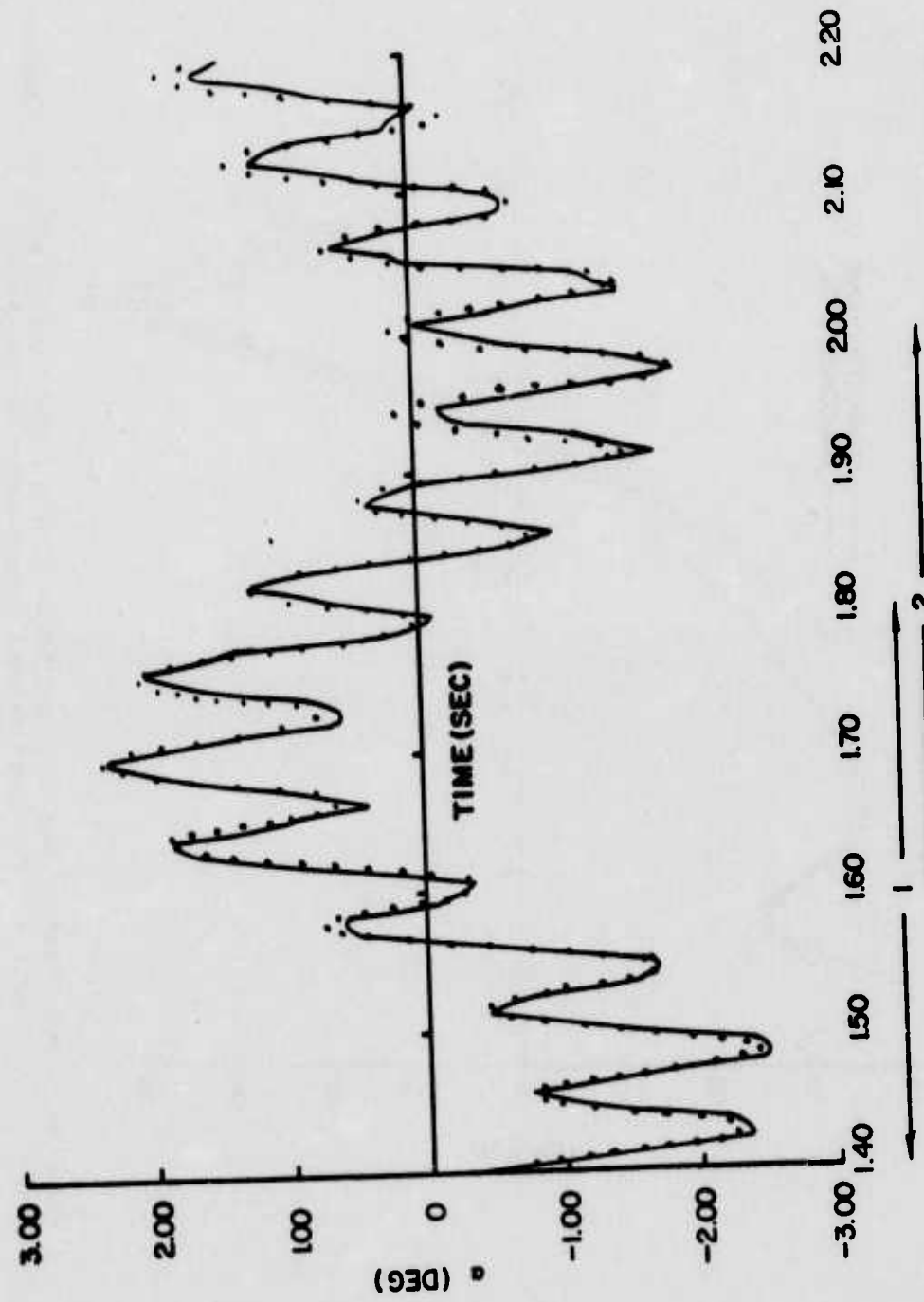


FIGURE 37 CHAPMAN-KIRK FIT TO ANGLE OF ATTACK DERIVED FROM AN INSTRUMENTED FLIGHT OF THE BOAT TAILED PROJECTILE

REFERENCES

1. E. J. McShane, J. L. Kelly, and F. V. Reno, *Exterior Ballistics*, University of Denver Press, 1953.
2. C. H. Murphy, "Free Flight Motion of Symmetric Missiles," Ballistic Research Laboratories Report No. 1216, July 1963, AD 442757.
3. W. K. Rogers, Jr., "The Transonic Free Flight Range," Ballistic Research Laboratories Report No. 1040, June 1958, AD 200177.
4. Aeronautics Panel of Aeronautics and Astronautics Coordinating Board of Department of Defense and NASA, "National Wind Tunnel Summary," July 1961.
5. *NASA Wallops Station Handbook*, April 1964
6. A. Platou, R. Colburn, and J. Pedgonay, "The Design and Dynamic Balancing of Spinning Models and a Testing Technique for Obtaining Magnus Data in Wind Tunnels," Ballistic Research Laboratories Memorandum Report No. 2019, October 1969, AD 699803.
7. W. R. Haseltine, "Yawing Motion of a 5.0" MK41 Projectile Studied by Means of Yaw Sondes," NWC TP4779, August 1969.
8. I. O. F. Amery, H. G. E. Henning, K. G. A. Lawrie, and E. J. M. Wlatnig, "A Telemetry System for the Measurement of the Yaw of a Projectile Throughout the Major Part of Its Trajectory (U)," RARDE, Gun and Ammunition Division Report No. 1/65, Fort Halsted, Kent, United Kingdom, (CONFIDENTIAL).
9. W. H. Mermagen, "Measurement of the Dynamical Behavior of Projectiles Over Long Flight Paths," AIAA Paper No. 70-538, AIAA Atmospheric Flight Mechanics Conference, Tullahoma, Tennessee, May 1970.
10. C. H. Murphy, "Data Reduction for the Free Flight Spark Ranges," Ballistic Research Laboratories Report No. 900, February 1954, AD 35833.
11. C. H. Murphy, "The Measurement of Non-Linear Forces and Moments by Means of Free Flight Tests," Ballistic Research Laboratories Report No. 974, February 1956, AD 93521.
12. R. F. Lieske and R. L. McCoy, "Equations of Motion of a Rigid Projectile," Ballistic Research Laboratories Report No. 1244, March 1964, AD 441598.

REFERENCES (continued)

13. P. Tunnel, "An Investigation of Sting Support Interference on Base Pressure and Forebody Chord Force at Mach Numbers from .60 to 1.30," NACA RM A54K16, January 1955.
14. E. Love, "A Summary of Interference at Transonic and Supersonic Speeds," NACA RM L53K12, January 1954.
15. D. Zonars, "Large Angle of Attack Model-Sting Interference Effects at Transonic Speeds," AGARD Report 301, March 1959.
16. G. T. Chapman and D. B. Kirk, "A New Method for Extracting Aerodynamic Coefficients from Free Flight Data," *AIAA Journal*, Vol. 8, No. 4, April 1970, pp. 753-758.
17. R. H. Whyte and A. Jeung, "Aerodynamic Reduction of Free Flight Transonic Range Data Utilizing Numerical Integration," General Electric Company Report No. 71APB514, April 1971.
18. R. H. Whyte, ""SPINNER" a Computer Program for Empirically Predicting the Aerodynamic Characteristics of Spin Stabilized Projectiles," Picatinny Arsenal Engineering Sciences Laboratory Information Report, September 1968.

LIST OF SYMBOLS

d	Model diameter, ft
g	Acceleration due to gravity, 32.2 ft/sec ²
p	Roll rate of the model, rad/sec
q, r	Transverse angular velocities of the model, rad/sec (for most exterior ballistic uses, $q \doteq \dot{\alpha}$ and $r \doteq -\dot{\beta}$)
q_t	$= (q^2 + r^2)^{1/2}$
$(C_i)^*$	$= \frac{\rho S d}{2m} C_i$
C_D	$= \frac{\text{Drag Force}}{Q S}$, Drag coefficient
C_{D_0}	Drag coefficient at zero yaw
C_L	$= \frac{\text{Lift Force}}{Q S}$, Lift coefficient (Positive coefficient: Lift force is in the plane of total angle of attack and normal to the trajectory in the positive direction of the total angle of attack.)
C_{L_α}	$= C_L / \sin \alpha_t$, Lift coefficient slope, 1/rad
C_M	$= \frac{\text{Static Moment}}{Q d S}$, Static moment coefficient (Positive coefficient: Moment increases the angle of attack.)
C_{M_p}	$= \frac{\text{Magnus Moment}}{Q d S (pd/V)}$, Magnus moment coefficient (Positive coefficient: Moment rotates the nose of the model normal to the plane of the total angle of attack in the direction of roll.)
$C_{M_p\alpha}$	Magnus moment coefficient slope, 1/rad
C_{M_α}	Static moment coefficient slope, 1/rad

LIST OF SYMBOLS (continued)

$C_{M_d} + C_{M_\alpha}$	=	<u>Damping Moment</u> $Q d S (q_t d/V)$, Aerodynamic damping coefficient (Positive coefficient: Moment increases the angular velocity of the model.)
C_N	=	<u>Normal Force</u> $Q S$	Normal force coefficient (Positive coefficient: Normal force is in the plane of the total angle of attack and normal to the model in the positive direction of the total angle of attack.)
I_x, I_y		Axial and transverse moments of inertia, respectively, $lb \cdot ft^2$	
M	=	$\left(\frac{md^2}{I_y}\right) (C_{M_\alpha})^*$	
Q	=	$\frac{1}{2} (\rho V^2/g)$, Dynamic pressure, psi	
R	=	τ_2 / τ_1 , Telemetry-pulse spacing ratio	
S	=	$\pi d^2/4$, Model reference area, ft^2	
T	=	$(C_{L_\alpha})^* + \left(\frac{md^2}{I_x}\right) (C_{M_{p_\alpha}})^*$	
V		Model velocity, ft/sec	
α, β		Angles of attack and side slip, respectively, rad	
α_t		Total angle of attack, rad	
δ	=	$\sin \alpha_t$	
θ		Trajectory angle with respect to horizontal, deg	
λ		Exponential damping factor, 1/cal	
ρ		Air density, lb/ft^3	
σ_n		Solar aspect angle, deg	
τ_1		Spin period, sec	

LIST OF SYMBOLS (continued)

Time between consecutive pulses, sec

τ_2

DISTRIBUTION LIST

<u>No. of Copies</u>	<u>Organization</u>	<u>No. of Copies</u>	<u>Organization</u>
2	Commander Defense Documentation Center ATTN: DDC-TCA Cameron Station Alexandria, VA 22314	1	Commander US Army Materiel Command ATTN: AMCRD-H 5001 Eisenhower Avenue Alexandria, VA 22333
1	Commander US Army Materiel Command ATTN: AMCDMA-ST 5001 Eisenhower Avenue Alexandria, VA 22333	1	Commander US Army Materiel Command ATTN: AMCRD-W, Mr. Happie 5001 Eisenhower Avenue Alexandria, VA 22333
1	Commander US Army Materiel Command ATTN: AMCRD-A 5001 Eisenhower Avenue Alexandria, VA 22333	1	Commander US Army Aviation Systems Command ATTN: AMSAV-E 12th and Spruce Streets St. Louis, MO 63166
1	Commander US Army Materiel Command ATTN: AMCRD-T, T. Shirata 5001 Eisenhower Avenue Alexandria, VA 22333	1	Director US Army Air Mobility Research and Development Laboratory Ames Research Center Moffett Field, CA 94035
1	Commander US Army Materiel Command ATTN: AMCRD-R 5001 Eisenhower Avenue Alexandria, VA 22333	3	Commander US Army Electronics Command ATTN: AMSEL-RD AMSEL-TL/I, J. Jacobs SELRA-SMA, M. Lowenthal Fort Monmouth, NJ 07703
1	Commander US Army Materiel Command ATTN: AMCRD-MT 5001 Eisenhower Avenue Alexandria, VA 22333	1	Commander US Army Missile Command ATTN: AMSMI-R Redstone Arsenal, AL 35809
1	Commander US Army Materiel Command ATTN: AMCRD-DN 5001 Eisenhower Avenue Alexandria, VA 22333	1	Commander US Army Tank Automotive Command ATTN: AMSTA-RHFL Warren, MI 48090

DISTRIBUTION LIST

<u>No. of Copies</u>	<u>Organization</u>	<u>No. of Copies</u>	<u>Organization</u>
2	Commander US Army Mobility Equipment Research & Development Center ATTN: Tech Docu Cen, Bldg. 315 AMSME-RZT Fort Belvoir, VA 22060	1	Commander US Army Natick Laboratories ATTN: AMXRE, Dr. D. Sieling Natick, MA 01762
1	Commander US Army Armament Command ATTN: AMSAR-SA, B. Witherspoon Rock Island, IL 61202	1	Commander US Army Training & Doctrine Command ATTN: ATCD-CF, LTC R.E. Camp Fort Monroe, VA 23651
2	Commander US Army Frankford Arsenal ATTN: SARFA-MDP, Mr. Mitchell SARFA-MDA-A, Mr. Hirshman Philadelphia, PA 19137	1	Commander US Army Field Artillery School ATTN: CPT J. Harnish Fort Sill, OK 73503
2	Commander US Army Picatinny Arsenal ATTN: SARPA-FR-S-A Mr. Loeb Mr. Kline Dover, NJ 07801	1	Commander US Army Research Office ATTN: CRD-AA-EH P. O. Box 12211 Research Triangle Park, NC 27709
1	Commander US Army Watervliet Arsenal Watervliet, NY 12189	1	Director US Army Advanced BMD Technology Center P. O. Box 1500 Huntsville, AL 35809
6	Commander US Army Harry Diamond Labs ATTN: AMXDO-TI Dr. M. Apstein AMXDO-DBC, Mr. T. Liss AMXDO-DAC, F. Vrataric AMXDO-DAD, D. Finger AMXDO-DAB, H. Davis 2800 Powder Mill Road Adelphi, MD 20783	1	HQDA (DAMA-DDC; LTC J. Ganahl) Washington, DC 20310
1	Commander US Army Materials and Mechanics Research Center ATTN: AMXMR-ATL Watertown, MA 02172	1	HQDA (DAMO-ZD, E. Smith) Washington, DC 20310
		3	Commander US Naval Air Systems Command ATTN: AIR-604 Washington, DC 20360
		3	Commander US Naval Ordnance Systems Command ATTN: ORD-0632 ORD-035 ORD-5524 Washington, DC 20360

DISTRIBUTION LIST

<u>No. of Copies</u>	<u>Organization</u>	<u>No. of Copies</u>	<u>Organization</u>
1	<p>Director Office of Naval Research ATTN: Mr. S. Curley 495 Summer Street Boston, MA 02210</p>	2	<p>ADTC (ADBPS-12) Eglin AFB, FL 32542</p>
5	<p>Commander US Naval Surface Weapons Center ATTN: GBJ, Mr. R. Kapnick Mr. E. Ohlmeyer KBB, Mr. J. Hurtt Dr. T. Clare DG-44, Dr. W. Chadwick Dahlgren, VA 22448</p>	2	<p>AFATL (DLRA, Mr. F. Burgess; Tech Lib) Eglin AFB, FL 32542</p>
6	<p>Commander US Naval Surface Weapons Center ATTN: Code 031, Mr. K. Lobb Code 512, Mr. R. Regan Mr. S. Hastings Code 730, Tech Lib Mr. D. Merritt Mr. P. Aronson Silver Spring, MD 20910</p>	1	<p>AFWL (SUL) Kirtland AFB, NM 87117</p>
2	<p>Commander US Naval Weapons Center ATTN: Code 753, Lib Code 50704 Dr. W. Haseltine China Lake, CA 93555</p>	1	<p>AFFDL Wright-Patterson AFB, OH 45433</p>
3	<p>Director US Naval Research Laboratory ATTN: Tech Info Div Code 770, Dr. A. Kolb Code 7720, Dr. E. McLean Washington, DC 20390</p>	1	<p>ARD (ARIL) Wright-Patterson AFB, OH 45433</p>
3	<p>Commander US Naval Ordnance Station ATTN: Mr. D. Monetta Mr. W. Burnett Mr. A. Hauckland Indian Head, MD 20640</p>	1	<p>ASD (ASAMCC) Wright-Patterson AFB, OH 45433</p>
		1	<p>Environmental Sciences Services Administration ATTN: Code 82.70, J.W. Wright Boulder, CO 80301</p>
		1	<p>Director National Bureau of Standards ATTN: Tech Lib US Department of Commerce Washington, DC 20234</p>
		1	<p>Director National Aeronautics and Space Administration Goddard Space Flight Center ATTN: Tech Lib Greenbelt, MD 20771</p>
		5	<p>Director National Aeronautics and Space Administration Ames Research Center ATTN: Mr. D. R. Harrison Mr. T. Canning Dr. D. Kirk Dr. G. T. Chapman Dr. M. Tobak Moffett Field, CA 94035</p>

DISTRIBUTION LIST

<u>No. of Copies</u>	<u>Organization</u>	<u>No. of Copies</u>	<u>Organization</u>
1	Director Jet Propulsion Laboratory ATTN: Tech Lib 4800 Oak Grove Drive Pasadena, CA 91103	1	Director National Aeronautics and Space Administration Scientific and Technical Information Facility ATTN: SAK/DL P. O. Box 33 College Park, MD 20740
1	Director National Aeronautics and Space Administration Langley Research Center ATTN: MS 185, Tech Lib Langley Station Hampton, VA 23365	3	ARO, Inc. ATTN: Tech Lib (2 cys) PWT-HTP, D. Herron Arnold AFB, TN 37389
5	Director National Aeronautics and Space Administration Wallops Station ATTN: Mr. R. Krieger Mr. C. Layton Mr. J. Green Mr. J. Andre Mr. W. Lord Wallops Island, VA 23337		<u>Aberdeen Proving Ground</u> Marine Corps Ln Ofc Dir, USAMSAA ATTN: Dr. J. Sperrazza Mr. C. T. Odom Cdr, USAEA ATTN: SAREA-R, Mr. A. Flatou Cdr, USATECOM ATTN: AMSTE-BE, Mr. Morrow AMSTE-TA-R, Mr. Wise